Investigation of Plasma-Assisted Nanoparticle Production at the Liquid-Solid Interface

Bachelor Thesis

in the
degree program
„Bachelor of Science“
in Physics

at the Faculty of Physics and Astronomy
of the Ruhr-Universität Bochum

by
Oliver Robert Krettek

from
Moers

Bochum 2023

March 29, 2023
by Oliver Robert Krettek
oliver.krettek@ruhr-uni-bochum.de
Faculty of Physics and Astronomy of the Ruhr-Universität Bochum
Experimental Physics II - Reactive Plasmas
Supervisor: Prof. Dr. Achim von Keudell

Deutsche Zusammenfassung

Mit Hochspannung betriebene gepulste Nanosekundenplasmen bieten ein breites Spektrum an Anwendungsmöglichkeiten in den verschiedensten Bereichen, zum Beispiel zur Reinigung von Abwasser [1], das Zersetzen von Textilfarbstoffen [2] und die Produktion von Nanopartikeln [3]. Nanopartikel haben ebenfalls ein breites Anwendungsgebiet, zum Beispiel in der Optik [4] oder der Medizin [5]. Die Nanopartikelproduktion auf herkömmliche Weise, zum Beispiel über photochemische oder elektrochemische Prozesse, kann bereits durch kleine Veränderungen im Prozess zu völlig verschiedenen Größen und damit Eigenschaften der Nanopartikel führen. Mittels verschiedener Verfahren wurde in dieser Arbeit die Herstellung von Nanopartikeln an der Flüssigkeits-Festkörper-Grenzfläche mithilfe eines gepulsten Nanosekundenplasmas untersucht. Dieses Verfahren ist gekennzeichnet durch einen einfachen Aufbau und damit der Möglichkeit, eine feine Größenverteilung der Nanopartikel vereinfacht zu erreichen. Die Nanopartikel stammen aus der Erosion der gepulst betriebenen Elektrode. Die Theorien zur Entstehung und Bildung der Nanopartikel liefern verschiedene Modelle, die aber aufgrund der kurzen Zeitskala im Nanosekundenbereich in diesem Projekt und der räumlichen Dimension von einigen Nanometern, mit aktuellen Diagnostiken nur schwer zu beweisen sind.

Nanopartikel in verschiedenen Größen konnten beobachtet werden. Die gemessenen Erosionen der Elektroden, welche zur Nanopartikel-Produktion führen, sind in Einklang mit den gemessenen dissipierten Energien und zeigen, dass für höhere Spannungen, die durchschnittliche Erosionsrate höher ist und damit die Nanopartikeldichte ebenfalls größer ist. Nur die durchschnittliche Erosionsrate ist größer, da diese von der Form der unbehandelten Elektrode abhängt. Die spitze Form hat ein höheres elektrisches Feld an der Spitze und damit mehr Plasmazündungen, was zu einer größeren Erosion führt. Die Nanopartikel konnten in nennenswerten Mengen nur für hohe Spannungen ab 22 kV beobachtet werden und wiesen Unterschiede zwischen positiver und negativer Polarität des Pulses auf. Für positive Pulse konnte eine schmale Größenverteilung im Bereich von 5 nm für gleichmäßig verteilte Nanopartikel gefunden werden. Für negative Pulse konnten nur unregelmäßig gefortme Cluster und Nanopartikel mit Größen bis 50 nm gefunden werden. Mit diesem Setup ist es insgesamt möglich, Nanopartikel einheitlich herzustellen, wenn auch nicht in der erwarteten Anzahl.

English abstract

Pulsed nanosecond plasmas operated with high voltage offer a wide range of applications in different fields, for example waste water treatment [1], decomposition of textile dyes [2] and the production of nanoparticles [3]. Nanoparticles are used successfully in many different areas, e.g. optics [4] or medicine [5]. The conventional production of nanoparticles via photochemical or electrochemical processes is very fragile and can lead to very different sizes and thus properties of the nanoparticles by small changes in the process. Using different diagnostics, the production of nanoparticles at the liquid-solid interface with a pulsed nanosecond plasma was investigated. This process is characterised by a simple setup and with that, the possibility to achieve a narrow size distribution of the nanoparticles more easily. The nanoparticles come from the pulsed treated electrode. The theories describing the formation of nanoparticles provide various models, but those are difficult to prove with current diagnostics due to the short time scale in the nanosecond range for this project and the spatial dimension of only a few nanometers.

Nanoparticles of different sizes were observed. The measured erosions of the electrodes, which lead to the production of the nanoparticles, are in accordance with the measured dissipated energy and show, that for higher voltages, the average erosion is higher and thus the nanoparticle density is also higher. It is only the average erosion rate that is higher, because of the shape of the untreated electrode. The pointy shape has a higher electric field at the tip and thus has more ignitions of the plasma, leading to a higher erosion. The nanoparticles could only be observed in significant quantities for high voltages up from 22 kV and showed a difference between positive and negative polarity. For positive pulses, a narrow size distribution with many evenly distributed nanoparticles at the size around 5 nm was found. For negative pulses, only irregular clusters and also nanoparticles with sizes up to 50 nm were found. It is possible with this setup to produce uniform nanoparticles, although not in as high quantities as expected.

Contents

Abstract iii

1 Introduction 1
- 1.1 Motivation . . . 1
- 1.2 Aim . . . 1

2 Theoretical Background 3
- 2.1 Pulsed plasma discharges in liquids . . . 3
  - 2.1.1 Setups for pulsed plasmas in liquids . . . 3
  - 2.1.2 Discharge types . . . 3
  - 2.1.3 Ignition mechanisms . . . 4
  - 2.1.4 Dissipated energy . . . 6
- 2.2 Nanoparticle Production . . . 7
  - 2.2.1 Nanoparticle production with pulsed ns discharges in water . . . 7
  - 2.2.2 Electrode Erosion . . . 8
  - 2.2.3 Laser Ablation . . . 8

3 Experimental Setup and Diagnostics 11
- 3.1 Experimental Setup . . . 11
- 3.2 Diagnostics . . . 12

4 Results and discussion 15
- 4.1 Power Measurements . . . 15
- 4.2 Erosion rates . . . 18
- 4.3 SEM Images . . . 24
- 4.4 TEM Images . . . 29
- 4.5 Laser Ablation . . . 31

5 Conclusion and outlook 35

A Appendix 37

Bibliography 39

Danksagung 43

1 Introduction

1.1 Motivation

A pulsed nanosecond discharge is generated by immersing electrodes into a liquid and applying an electrical current. Pulsed nanosecond discharges in water have attracted more and more attention in the last years due to their wide field of applications, which include wastewater treatment [1], breakdown of textile dyes [2], sterilisation [6] as well as nanoparticle production [3].
Nanoparticles have many applications, for example in optics [4], medicine as antibacterials [5] and biology [7]. The conventional way of nanoparticle production with e.g. photo-chemical [8] or electro-chemical processes [9] is very sensitive to external factors like pressure or temperature. Just the smallest changes in the processes can lead to entirely different sizes and size distributions and with that, to very different properties which may or may not be of particular interest [10].
Pulsed nanosecond plasmas in liquid are a possible simplification of this process, as they provide a rather straightforward setup, because there is no need for vacuum equipment and there are less production steps. This could allow the scale up for mass production. The nanoparticles are produced via the erosion of the electrode material per plasma pulse.
A different approach uses laser ablation to erode a target material in a liquid, during this process a plasma is also ignited [11].

1.2 Aim

The aim of this thesis is to show how the electrode erosion rate is related to the production of nanoparticles. It is expected that for increasing voltage, the erosion rate and thus the nanoparticle production increases. The variable parameters are voltage, treatment time, polarity of the pulse as well as the material the electrode is made out of.
The analysis of the production rate will be done with shadowgraphy images of the electrode tip. Additionally, power measurements will be done. The produced nanoparticles will be analyzed with transmission electron microscopy (TEM) and the electrode tips will be analysed with scanning electron microscopy (SEM). In addition, the production of nanoparticles via laser ablation will be compared to the production via erosion of electrodes.

With those measurements, it will be possible to characterise this particular setup for its efficiency of nanoparticle production.

This thesis was written within the framework of the *SFB1316 Project B7: Reaction chemistry of plasmas in liquids interacting with surfaces.*

2 Theoretical Background

The investigation of plasmas and their ignition in liquids is a challenging subject because many different fields of physics play a role together: obviously plasma physics as well as quantum mechanics, hydrodynamics, thermodynamics and complex interactions at the gas-liquid-solid interfaces. Into all of this falls the formation and production of nanoparticles. This chapter sets up the needed theoretical background and is divided into two main sections: Section 2.1 focuses on plasma discharges in liquids and their ignition mechanisms and section 2.2 deals with the nanoparticle production of plasmas in liquids.

2.1 Pulsed plasma discharges in liquids

2.1.1 Setups for pulsed plasmas in liquids

As for the configuration of the setup for pulsed plasmas in liquids, there are many different realisations, as thoroughly discussed by Bruggemann et al. in [12]. It is convenient to divide those setups into three main categories: direct discharge in liquid, gaseous discharges above a liquid and gaseous discharges in bubbles inside a liquid. Typically, pin and plane electrodes are used. The setups are shown in figure 2.1. The setup in this thesis is a Pin-to-Pin configuration.

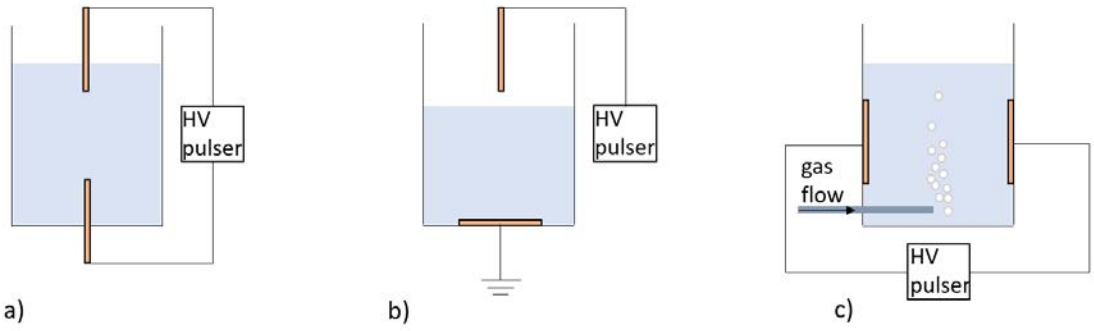

Figure 2.1: Illustration of different configurations for discharges in liquids, adapted from [12]. Part a) shows a Pin-to-Pin configuration submerged in the liquid, b) one electrode above the surface of the liquid while the other plane electrode is submerged and grounded and c) shows a setup with a bubbler between the plane electrodes.

2.1.2 Discharge types

It is possible to distinguish different types of discharges for plasmas in liquids as discussed by Brugemann et al. in [13]. In literature, a distinction is made between these types of discharges:

- **Corona-like**: these discharges are created by the strong and inhomogeneous electric fields. These electric fields cause a breakdown in the liquid. The plasma does not reach the other electrode, although current flows into the liquid. Corona-like discharges glow around the electrode tip.
- **Streamer-like** discharges are created the same way corona-like discharges are. The only difference is, that so called streamers are formed and enter the liquid further than the glow around corona-like discharges.
- **Spark- and Arc-discharge**: those discharges reach the opposite electrode. This leads to a way higher erosion of the electrodes compared to the corona- and streamer-like discharges. For plasmas in liquids, those discharge types are used quite rare [14].

For the particular setup used in this thesis, a streamer-like discharge is observed, as shown by Grosse et al. in [15].

2.1.3 Ignition mechanisms

In this thesis, the plasma is pulsed in the nanosecond range. This is important because for different timescales, the plasma ignition happens through other mechanisms.
Plasma ignition in liquids can only take place if a certain threshold of voltage per surface area is reached. Only then the electric field is strong enough. So it is convenient to either decrease the surface area of the electrode or increase the voltage, in best case both. This explains the more common use of pin electrodes, as in e.g. [16]. The relation between the electric field E, voltage U and the radius r_E of the semi-spherical electrode tip is approximated as

$$E = \frac{U}{5 \cdot r_\mathrm{E}} \tag{2.1}$$

according to [17]. Alternatively, it can also be approximated as

$$E = \frac{2U}{r_\mathrm{E} \cdot \ln(\frac{4d}{r_\mathrm{E}})} \tag{2.2}$$

according to [18]. Here, d is the distance between the electrodes and in this thesis can be approximated as $d \approx 1$ cm.
Pulsed plasmas in the microsecond range with relatively high rise times of more than 10 ns have already been studied extensively [13]. For those, Korobeinikov et al. found out that the plasmas ignite in gas bubbles that are created via joule heating [19]. For pulsed plasmas in the nanosecond range with short rise times of a few nanoseconds or less, there is not enough time for joule heating and the plasma ignites directly in the liquid [13]. The ignition mechanisms are still discussed and not fully understood. Additionally, there is a lack of experimental proofs for the mechanisms due to the fact that the short rise times make it very challenging as mentioned by Grosse et al. and Seepersad et al. [18, 20]. According to Nominé et al. [3], the plasma ignites in the following way: When the current is applied, first there is a pre-breakdown phase. Charges are injected into the liquid coming from the electrode(s). These charges can be electrons coming from the cathode or impurities inside the liquid are split into ion pairs of opposite charge at the anode. These charges inside the liquid drive an electrohydrodynamic movement which leads to a turbulent flow. The formation of regions of low density can lead to the breakdown, when the density is low enough for charge multiplication or electron avalanches. The discharge ignites and if the dissipated power is high enough, even a shock wave in the range of GPa can form [3, 21]. Other possible mechanisms will be discussed next.

Gaseous bubbles

Evaporation or dissolved air can lead to the occurrence of gas bubbles inside the liquid, especially if the water is placed inside the ignition chamber before plasma ignition for a longer period of time. In those bubbles that are near the electrode, electron chain reactions can ignite the plasma the same way plasmas are ignited in gases. The discharge then would behave the same way as a discharge in gas.

Field effects

Field effects appear with high electric fields. It is necessary to distinguish between the polarity of the electrode: for positive voltages, field ionisation takes place while for negative voltages, the field emission of electrons happens. The effect of field emission occurs because of the high electric field which shifts the potential barrier or tunneling barrier between the liquid (water) and solid (electrode) phase. It is then possible for the electrons at the electrode tip to tunnel out of the electrode and cause the chain reaction for ignition. For the positive voltage, the opposite case happens: electrons from the water molecules in the direct volume around the electrode tip tunnel directly into the electrode because of the energy barrier shift.
The needed electric field strengths for field effects to occur depend on the materials at the liquid-solid interface. For a high enough probability for field ionisation of tungsten to occur, field strengths of $E \approx 0.2\,\mathrm{V\ \AA^{-1}}$ are needed, while for a platinum/iridium alloy the threshold lies between $E \approx (0.5-0.6)\,\mathrm{V\ \AA^{-1}}$, according to [22]. For field emission, electric field strengths of $E \approx (0.3-0.6)\,\mathrm{V\ \AA^{-1}}$ are necessary [17].

Nanovoids

The theory of nanovoids utilises the high electric field at the electrode tip. Due to this, electrostriction occurs in the surrounding volume. The short rise times of the pulses then cause a rupture in the liquid, in which a very low density or even a vacuum can be created. Here the electrons can be accelerated by the electric field and have a long enough free mean path to cause ionisation. The nanovoids have a spatial dimension of a few nanometers. However, theoretical calculations by Stauss et al. show that these scales are not enough to explain why a plasma ignites [23]. The electron chain reaction can not happen in the nanovoid, but individual electrons could be accelerated enough and hit water molecules on the border of the nanovoid, where they would release several electrons and trigger the electron chain reaction that ignites the plasma. Figure 2.2 shows an illustration of this.
Experimental proof of nanovoids is still missing. According to [24], it is possible that nanovoids and field effects together are the reason the plasma ignites.

Supercritical Fluid

When a liquid is heated above its critical point and put under immense pressure, it can reach the state of the supercritical fluid. Supercritical fluids have properties from both the gaseous phase, e.g. the viscosity, and the liquid phase, e.g. the density [23].
The supercritical fluid model suggests that near the electrode tip, where high pressures and temperatures occur, the water is not in the liquid phase, but rather in a supercritical state. Water reaches the supercritical state at $T_c = 647$ K, $p_c = 22.1$ MPa and $\rho_c = 0.32$ g/cm^3 [25]. Those critical values have been greatly surpassed in nanosecond plasmas, where temperatures of several thousands Kelvin and pressures in the GPa range are created, as observed by Grosse

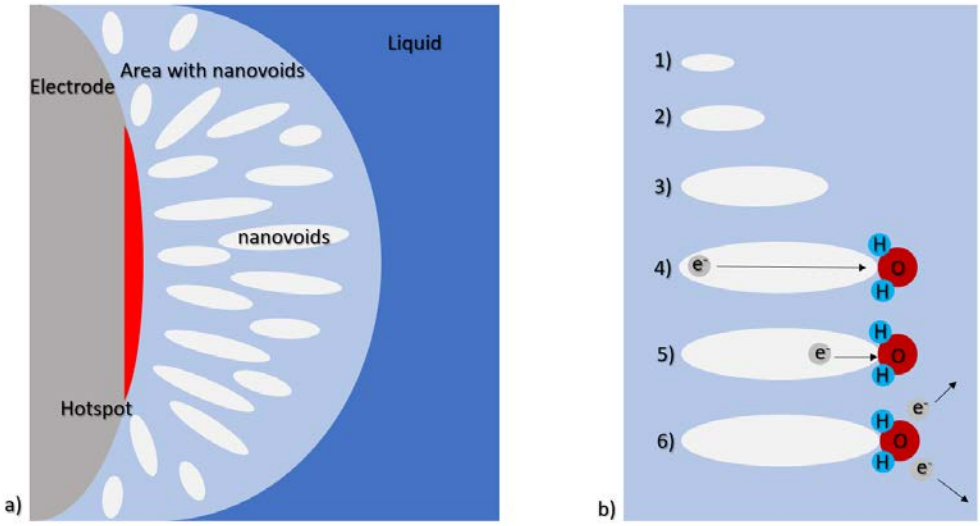

Figure 2.2: Illustration of a) the location and formation of nanovoids around the electrode tip and hot spot and b) the formation of nanovoids and the beginning of an electron chain reaction. Adapted from [18].

et al. [26]. Supercritical fluids have density fluctuations on a molecular level, which can lead to regions with low densities. In those regions the free mean path for the electrons is longer than in liquid water, and the electrons can be accelerated enough to ionise the water and ignite the plasma. When the liquid reaches the super critical state, the process leads to a chain reaction for the surrounding volume because of the high enough temperature and pressure at the center.

2.1.4 Dissipated energy

The estimation of the power and energy that is dissipated into the plasma happens according to [21]. Using the BCS signal, the dissipated power is:

$$P_{dissipated} = P_{initial} - P_{reflected} \tag{2.3}$$

with the power $P = U \cdot I$. The power losses in the cable can be calculated in the following way[21]: the power of a 20 kV pulse with a current of 450 A is P = 9 MW. Grosse determined the BCS power to be at $P_{BCS} = 54.7$ kW which accounts to be 0.6%, which is therefore negligible. The lost energy than can be determined by integration over time of equation 2.3 which leads to

$$E_{dissipated} = E_{initial} - E_{reflected}. \tag{2.4}$$

The analysis will be done with the same computer program used in [21]. The energy balance for discharges in liquids is according to Nominé et al. [3]:

- The creation of the plasma takes 95% of the energy.
- Roughly $\approx$ 5% dissipates with the bubble.
- Only $\approx$ 1% goes into the erosion of the electrode.
- Less than 0.1% goes into the shock wave.

2.2 Nanoparticle Production

Nanoparticles have been established and used in chemistry for years and can even be traced back to Michael Faraday, who produced gold colloids via the reduction of gold chloride with phosphorus in water [27] and is the first one to use the solution-phase for nanoparticle synthesis [28].
The chemical reactions for the production of metal nanoparticles are way simpler than for organic synthesis of e.g. production of drugs, because the complex organic molecules with seemingly endless structures are not involved. The difference to organic nanoparticle synthesis is the growth mechanism of the nanoparticles. Currently available information can not explain details in the formation of nanoparticles and the production is even described rather as art than science [28]. It is generally assumed that the formation of nanoparticles happens in three steps, which will be described next [28]:

- **Nucleation**: At the beginning of the formation, free metal ions are created. Typically, they are released from a precursor using heat. The concentration of atoms near the precursor can reach a saturation point, at which the atoms cluster together to form nuclei, consisting of just a few atoms. The growth rate of the nuclei even may increase during the release of more atoms. These nuclei are the first stage of formation of nanoparticles.
- **Seeds**: The nuclei clusters grow via the addition of atoms or even the direct merging of several nuclei clusters to a point at which structural fluctuations become energetically unfavourable. Now they have a well-defined structure and are called seeds, which is the intermediate step in this theory for formation. The structure of the seeds is defined by the free energies of statistical thermodynamics. The seeds already can consists of a few hundred atoms.
- **Nanoparticles**: The seeds can grow further through the addition of atoms. Those atoms, as is known from chemical deposition studies, need to find a place on the seeds where they can attach, such as a hole, step or edge. This growth process can continue further until a point is reached, where the seed now enters the dimension of nm and is called a nanoparticle. Of course, the growth can also happen through clustering of seeds. The growth process itself is dynamic: on one hand, there is the decreasing bulk energy which favours the growth of the seed, on the other hand there is the increasing surface energy which counteracts the growth.

2.2.1 Nanoparticle production with pulsed ns discharges in water

The production of nanoparticles with discharges inside of liquids is relatively new and has the huge advantage, that there are way less production steps and the setups are simpler than for conventional ways of production. For those, there are also different realisations for the productions: the two main ways are the production via the erosion of the electrode [16], where the material that forms the nanoparticles comes direct from the electrode and via plasma-chemistry, where reactions between plasma species and the liquid occur, as Ashkarran showed [10]. Applicable liquids can be for example water, benzene [14], ethanol or ethylene glycol [28] as well as other solutions [29]. The used setups have already been discussed in section 2.1.

2.2.2 Electrode Erosion

In context of this thesis, the nanoparticle production is done via the erosion of the electrode needle. The erosion can be explained by different mechanisms [3]:

- **Melting**: According to Hamdan et al. [30], the electrodes melt because of the irradiation of black body emission by the high temperatures of the discharge . The heated electrode emits a vapour into the liquid and the vapor later condensates, leading to the formation of nanoparticles. This can go hand-in-hand with the previously mentioned mechanism of nucleation.

- **Spallation**: The process of spallation describes the material ejection which is driven by the relaxation of the previously stressed material due to the treatment. It is a thermodynamic process and leads to nanoparticles in the size range of 10 nm.

- **Explosive Boiling**: The mechanism of explosive boiling or phase explosion works like this: a super-heated surface region of the electrode tip expands rapidly away from the rest of the electrode into the liquid, where it is then fastly decomposed into a mixture of vapor and liquid droplets consisting of the electrode material. The energy required for explosive boiling is much higher than for spallation and the size of produced nanoparticles lies also in the range of 10 nm. Additionally, there are also huge droplets produced.

As it strikes, there are plenty of different approaches to a theory behind the formation of nanoparticles. The problem is, that it is currently not possible to look with some kind of electron microscope or dynamic light scattering at this process for better understanding of it because of the short time scale and the small dimensions those processes happen in. It is quite possible that a combination of those theories and not just a single one could describe the formation of nanoparticles to a satisfying level.

2.2.3 Laser Ablation

For the synthesis of nanocrystals or nanoparticles, the process of laser ablation is considered to be very efficient and environmentally friendly, as stated by Taccogna and Amendola et al. [11, 31]. The laser parameters are the wavelength, duration and energy of the laser pulse. Also the repetition rate, the total number of pulses and the size of the area the laser hits are important parameters [31]. The process of laser ablation works as follows: after the laser beam hits the surface of the target, a small but expanding plasma is created. The plasma is expanding because it has a very high kinetic energy. The liquid environment confines the plasma and limits the expansion. The created plasma has a very high density and a fast decreasing temperature due to the high rate of recombination [11]. There are different proposed mechanisms that explain the formation of nanoparticles during the process of laser ablation. Amendola and Meneghetti [31] propose a mechanism that can be split into three different phases [31]:

1. In the first phase, the nucleation around ion-seeds from the target material that was ejected takes place. This is due to the confinement of the liquid. Nanoparticle embryos of a few atoms are formed.

2. In the second phase, the growth of the nanoparticles driven by the surrounding plasma takes place.

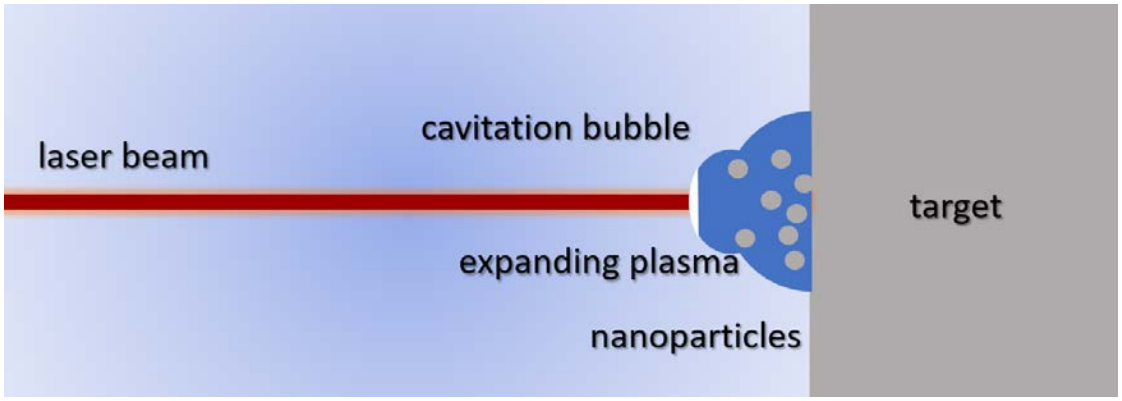

Figure 2.3: Illustration of the laser ablation process. The laser beam hits the target, where the plasma is created and expands (blue). At the tip of the expanding plasma, a cavitation bubble is formed (white). The atoms of the produced nanoparticles come from the target.

3. The last phase is the crystallisation of the formed nanoparticle and leaving the cavitation bubble into the liquid.

Another mechanism is described by Sasaki and Takada [32]: the first thing that happens after the laser hits the target is the ejection of particles from the target material. A cavitation bubble forms, the ejected particles are outside of the bubble. In [32], it was observed that the previously ejected particles are transported towards the cavitation bubble and the growth of the nanoparticles occurs inside the bubble. A great portion of those nanoparticles stays inside the cavitation bubble until it collapses, but some of the nanoparticles are ejected before within child bubbles. A proof for a mechanism is because of the small time scales and the dimension of the nanoparticles quite challenging and still missing.

3 Experimental Setup and Diagnostics

3.1 Experimental Setup

Before taking a look at the diagnostics used in this thesis, the experimental setup is described in the following.

In-liquid-chamber and electrodes

The ignition of the plasma takes place in the in-liquid-chamber shown in figure 3.1. The chamber is made out of polymethyl methacrylate (PMMA) and can contain up to 25 ml of liquid. For this thesis, distilled water is used. To fill the chamber with water, there are four in- and outlets with valves which also can be used for flow-measurements. In context of this thesis, the ignition only took place in stationary water. One of the valves is always open during ignition for pressure regulation. The distilled water has a conductivity of $\sigma \approx 1$ μS /cm. For optical measurements, the chamber has one big window made out of quartz glass on the front and two smaller windows at the same height on the sides. In this setup, a pin-to-pin configuration for the electrodes is chosen. The electrodes consist of copper rods embedded in tubes made of glass, into which stainless-steel canulas can be inserted. For the powered electrode, a 50 μm thin metal wire is attached into the canula. The length is adjusted so that it can be viewed via the two smaller windows in order to measure the erosion of the electrode using shadowgraphy images. The wire is also placed in such a way, that possible curvature of it lies in the same plane as the camera chip and so is visible. In context of this thesis, tungsten (W) and platinum/iridium (Pt/Ir) alloy wires from Goodfellow Cambridge Ltd. are used. The Pt/Ir alloy wire consists of 90% platinum and 10% iridium and has a purity of 99,94% and the tungsten wire has a purity of 99,95%. According to the manufacturer, the melting point of tungsten is 3410° C and the melting point of the platinum/iridium alloy is between 1830° C and 2120° C. The grounded electrode is a stainless-steel canula.

Pulse-Generators

Two different high voltage pulse generators from FID Technology GmbH are used, one for positive pulses and one for negative pulses. The positive pulse generator is FPG 30-01NK10, which can produce pulses of 10 ns in length with pulse rise times of 2 - 3 ns. The frequency can be changed from 1 - 100 Hz and the voltage amplitude from 10 - 30 kV. The positive pulser is connected to the electrodes with a RG217 coaxial cable of 6 m length. A back-current shunt (BCS) is integrated into the cable for voltage measurements.
The second pulse generator of model number FPG 30-01NK10-NEG is the negative pulser. It can generate pulses from -(10 - 30) kV and is connected with a 6 m RG217 coaxial cable mounted again with a BCS. The BCS-cable lengths are important to delay reflections in the signal. Those reflections are created at the electrodes because of an impedance mismatch. The reflected pulse could then arrive again at the electrode and influence the plasma, but with a cable length of 12 m or 6 m the reflected pulse would theoretically arrive back at the

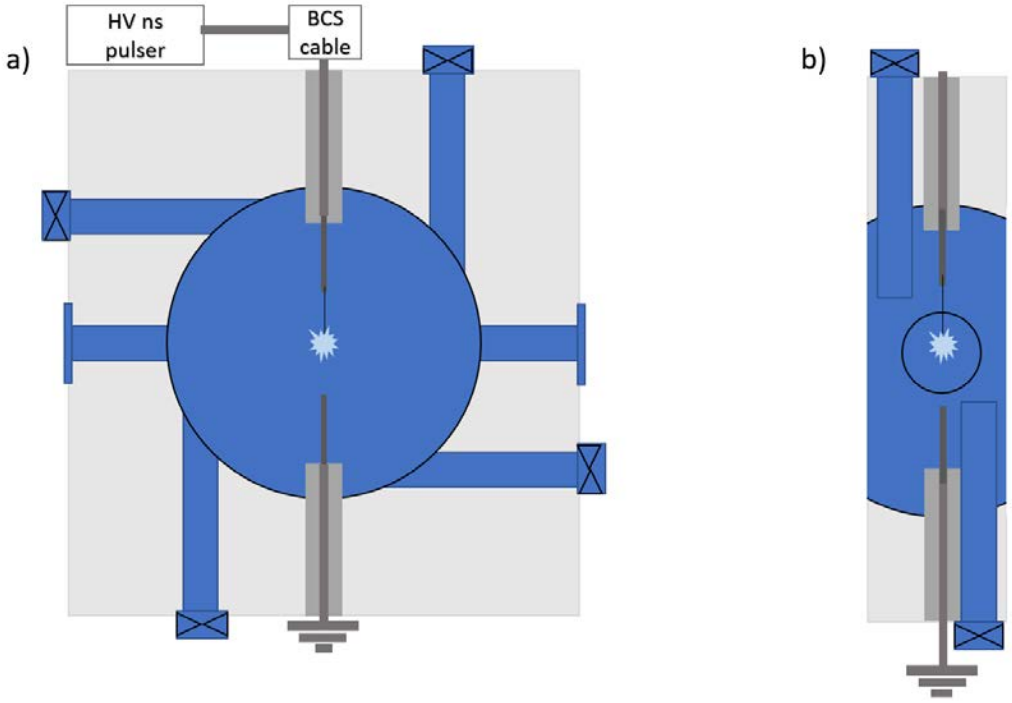

Figure 3.1: Illustration of the liquid chamber setup. a) shows the front view of the chamber connected to a pulser and b) shows the side view with the optical path for erosion measurements.

electrode after 120 ns or 60 ns, respectively. This is way too late to interfere with the initial pulse.
Because of the fast rise times of the voltage pulses, electromagnetic interference is induced. In order to avoid the influence of the electromagnetic interference on other electric instruments and devices, the pulser and the in-liquid chamber are enclosed in a Faraday cage. Outgoing cables, e.g. the power supply or for voltage measurements, are covered in ferrite cores to further reduce electromagnetic interference.

3.2 Diagnostics

Electrical Measurements

In order to obtain the energy dissipated in the plasma, a BCS cable is connected to an HD6104A oscilloscope from Teledyne LeCroy GmbH. Because the voltage pulses could possibly damage the oscilloscope, three attenuators, placed in series, are used that add up to an attenuation of 36 dB. With the data for voltage over time, the power that is dissipated can be calculated with a computer program, see [21].

Shadowgraphy imaging

For the erosion rate measurement, an intensified charge-coupled device (ICCD) camera is used. The model is an andor iStar ICCD camera (DH734-18U-03). A xenon arc-lamp is positioned facing towards a small window of the in-liquid chamber. The shadow of the wire is then focused with a lense of a focal length d = 12 cm onto the ICCD-camera which is connected to a computer for recording the images. A sketch of the setup is shown in figure 3.2.

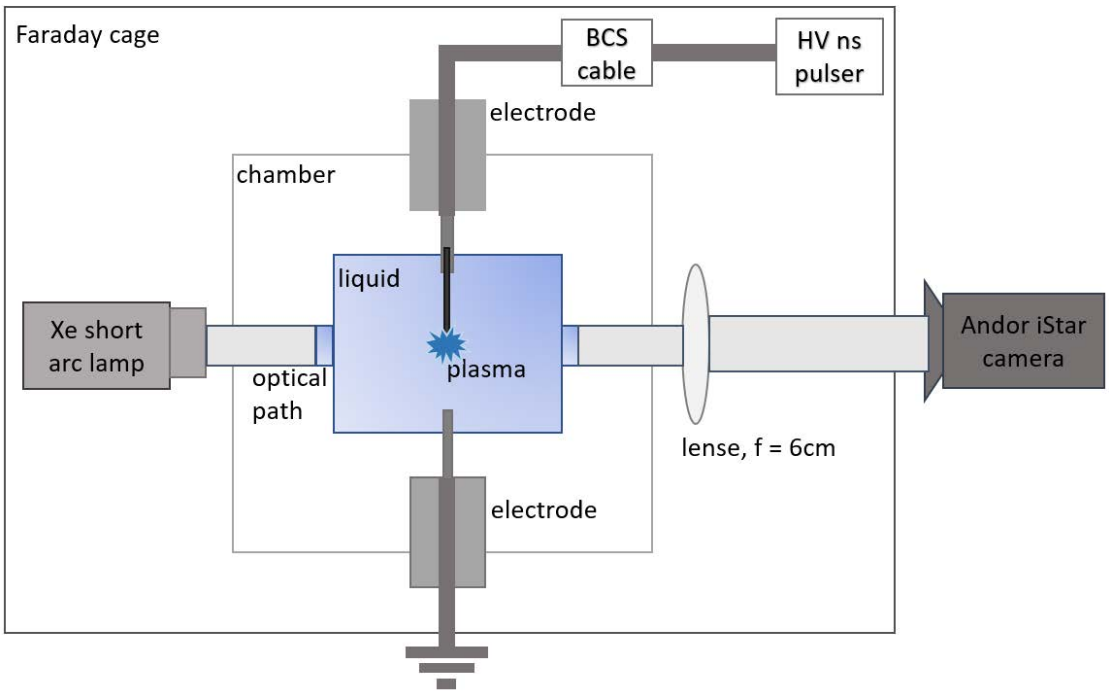

Figure 3.2: Illustration of the imaging setup. The xenon short arc-lamp casts its light through the optical path and a lense onto the CCD chip of the camera, where the shadow of the electrode tip is visible.

The idea for measuring the erosion rate is the following: the change in length of the electrode is observed over time. Images are then taken before, during and after ignition. Because of small micro explosions taking place where the plasma ignites and the electrode heats up, the position of the needle may vary. The images during ignition are because of that not single shots like in the static case of before and after ignition, rather accumulated shots. For the measurement of the erosion rate, this is not as important because the image of the shadow is blurry and there is no reference point for the measurement of the length of the wire. It is still important to take those images because the movement caused by the micro explosions can have a bias and change the relative position of the curvature of the wire. This could lead to wrong erosion rates.

Scanning Electron Microscopy

When looking at nanoparticle production, it is also interesting to take a look at the electrode tips because information can be obtained on the erosion or material removal from the surface of the electrode. For that, the electrode tips were analyzed before and after plasma treatment with environmental scanning electron microscopy (ESEM). In scanning electron microscopy, a sample is scanned with a focused electron beam. The interaction between the electrons and

the sample results in back radiation which is used to generate an image of the sample. In ESEM, the pressure in the chamber can go up to 1300 Pa while for the SEM a high vacuum is needed.
The used SEM model is JSM-7200F from Jeol and has a maximum beam current of more than 600 nA. The resolution lies between 1.6 nm at 1 kV acceleration voltage and 1 nm at 30 kV. The SEM is located at the Center for Interface-Dominated High Performance Materials (ZGH) at RUB. The images were taken by Pia Pottkämper.

Transmission Electron Microscopy

In contrast to SEM, where a focused electron beam is used, the transmission electron microscopy works the same way like conventional light microscopy. For TEM, the examined samples have to be very thin and so it is convenient to use it for analysing nanoparticles. The used TEM is a JEM-2800 with Schottky field emission cathode from Jeol which operates between 100 kV and 200 kV. For the obtained pictures in this thesis, the Schottky cathode was operated at 200 kV acceleration voltage. This results in a chromatic aberration of 1.3 mm and 0.7 mm spherical aberration. The point resolution is 0.2 nm.
The obtained samples of water after plasma treatment are prepared in the following way: the majority of the 25 ml was removed by rotary evaporation in vacuum which left a sample of around 1 ml. To that, 1 ml of ultra pure water was added. From this, 100 μl were drop-casted onto an ultrathin C film on Lacey carbon support film with a 400 mesh Cu grid. To find out that the observed things are really metallic nanoparticles, the contrast between those and the carbon support is used. The metallic nanoparticles are darker than the carbon support. The lattice is used to make metallic structures at high resolutions visible. With this analysis it is however not possible to determine the chemical composition of the nanoparticles.
The TEM is located at Center for Solvation Science (ZEMOS) at RUB. The images were taken by Paolo Cignoni.

Laser Ablation Setup

The experiment for Laser Ablation was done at the company Lidrotec GmbH in Bochum. The construction is described in the following: the laser beam went through several optical corridors to a scanner, with which it was possible to target a specific location on the target material. The laser impact always happens at an 90° angle and the target material was put under a foil and laminated with vacuum, to protect the setup from the water. For this system, 2 l of water were flowing over the target material and circulating within the setup. The laser operates at a wavelength of $\lambda = 1030$ nm in the infrared range and had a pulse duration of 350 fs. The target area was circular and had a diameter of 10 μm, but this does not equal necessarily the area that was removed. The laser operated at 15 Hz and deposited an energy of 3,07 J onto the area. The average power used was 440 mW. The laser could be moved manually between treatment, targetting one spot only during treatment.
As target material, quadratic foils with a side length of 1 cm are used. The used materials are the same as for the electrode wires: tungsten with a purity of 99,5% and a platinum/iridium alloy (platinum with 90% and iridium with 10%) with a purity of 99,4%. The thickness of the foils is 100 μm.
More details can not be provided due to a non-disclosure agreement signed with Lidrotec GmbH.

4 Results and discussion

In this section, the obtained measurements and results will be discussed. First comes the discussion of the power and dissipated energy for a basic understanding of the system before discussing the erosion rates. For better understanding of the erosion rate, the SEM images will be discussed thereafter before taking a look at the actual nanoparticles with TEM images. At the end, a quick comparison with the laser ablation process of nanoparticle production will be done.

4.1 Power Measurements

In order to understand the system, the first measurements done were the power and energy measurements to get a basic knowledge of how much energy actually goes into the plasma and nanoparticle production. These were done, as well as all other measurements, with the 6 m cable. This is due to the fact that the other cables were occupied and currently not available for measurements. A negative side effect of using this cable is that compared to the longer ones, the reflected pulses have shorter travel times and can interfere with the other pulses. A comparison between the 6 m cable and the 12 m cable is shown in figure 4.1. It is

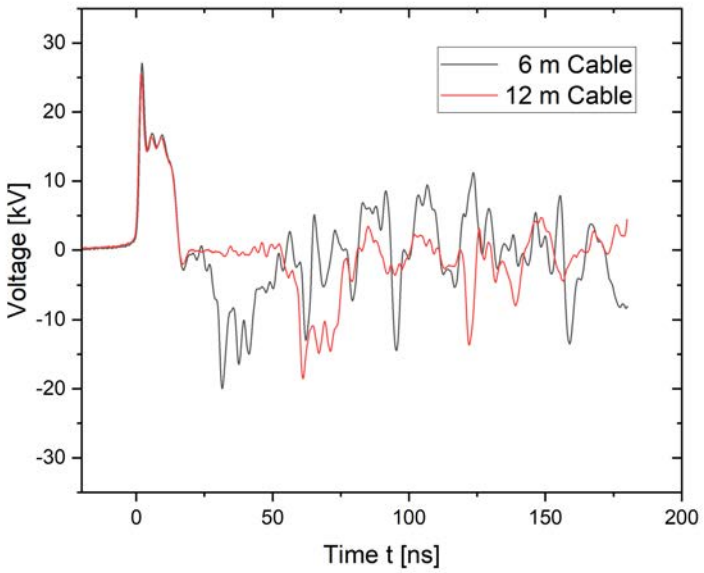

Figure 4.1: Comparison of the BCS signal for a +20 kV pulse with a tungsten electrode. The 6 m cable is shown in grey while the 12 m cable is shown in red. For the initial pulse, the signals are overlapping clearly. Because of the longer time before reflection, the reflected pulse and other oscillations do not line up.

also noticeable that the pulse begins with an overshoot above the set amount of voltage at the pulser and then drops to a plateau which is lower than the set voltage. The pulse width provided by the manufacturer of the power supply is about 10 ns long as can be verified in figure 4.1. The pulse shape differs however: the stated pulse shape is quadratic and does not have the overshoot and slight oscillations. This observed shape therefore originates from the setup.
A shape comparison of the pulses for positive and negative polarity from the different pulsers is shown in figure 4.2. The shapes are, especially for the first 30 ns to 40 ns, nearly identical and begin to change slightly during the reflected pulse. This is most probably caused by the setup, given that the pulse shapes already differ from the ones stated by the manufacturer.

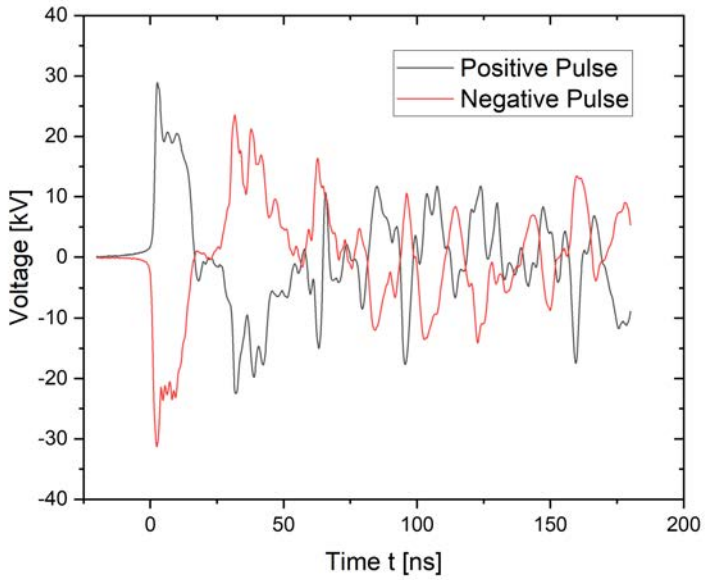

Figure 4.2: Comparison between a positive and negative 24 kV pulse using a platinum/iridium electrode. The pulses are very similar to each other, especially the initial and the beginning of the reflected pulse.

The dissipated energy is determined with a Matlab program written by Grosse [21]. The program works in the following way: the user chooses four different points manually at which he thinks that the first pulse begins and ends and where the reflected pulse begins and ends. The program used the calculation steps from section 2.1.4. The dissipated energies for tungsten and platinum/iridium for both positive and negative pulses are shown in figure 4.3.
A very simple model would predict that the dissipated power should have a quadratic growth according to

$$P = \frac{U^2}{R}. \tag{4.1}$$

The energy is then calculated by integration over time. This model is fairly too simple for the case in this thesis, nevertheless the growth of the dissipated energy is clearly visible. The obtained dissipated energies lie in the range of 10 mJ to nearly 40 mJ. Also interestingly, for the same material, the dissipated energies for positive and negative pulses at low voltages are nearly the same while for higher voltages, the dissipated energies diverge from each other, while the positive pulses dissipated more energy than the negative pulses. The error for the

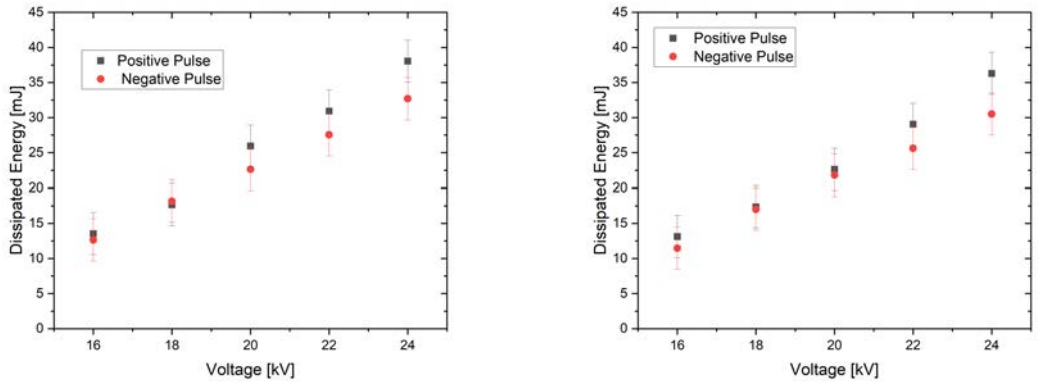

(a) (b)

Figure 4.3: Dissipated energies for (a) tungsten electrodes and (b) platinum/iridium electrodes.

dissipated energies was estimated to be $\Delta E_{diss} = \pm 3$ mJ. This is due to the fact that there is already interference between the reflected pulse and other signals and it was not easy to find where the reflected pulse actually ends.
Grosse used in her dissertation [21] the same setup and pulsers, but measured for the dissipated energy for a 20 kV positive pulse with a tungsten electrode only a dissipated energy of $E_{diss} = 2.5$ mJ which is one magnitude lower than what was measured in this thesis. The measured values were for tungsten $\approx (26 \pm 3)$ mJ and for platinum/iridium $\approx (23 \pm 3)$ mJ. One reason for this discrepancy may be the selection of the points in the program by the user, where the (reflected) pulse begins and ends. Additionally, Grosse used a 12 m cable for her power measurements and thus could have determined these points easier. However, Grosse only provided one measurement in [21] which may have an additional error in contrast to several measurements done within this thesis. Babicky et al. [33] measured for a 60 kV pulse a dissipated energy of $\Delta E \approx 100$ mJ. This value is, linearly interpolated, lower than what to expect from the measurements from this thesis. Due to Babicky et al. using a different setup and operating in a much higher voltage range, the obtained values for the dissipated energy nonetheless seem reasonable. Remembering from section 2.1.4, that only $\approx 1\%$ of the dissipated energy goes into the erosion of the electrode, we are in the range of 0.1 mJ to 0.4 mJ.

Now that there is a general idea about the dissipated energy in the system, it is possible to look what this dissipated energy leads to: erosion of the electrodes.

4.2 Erosion rates

With the knowledge of the dissipated energy, in this section the erosion rates E_r will be determined as mentioned in section 3.2. For that, the lengths L of the electrode are determined with the program ImageJ [34] before and after a specific time and this difference is divided by the number N of ignitions:

$$E_r = \frac{L_{before} - L_{after}}{N} \tag{4.2}$$

Additionally, the width of the electrode is measured for each image as means of reference. The error for the erosion rate is estimated with Gaussian error propagation:

$$\Delta E_r = \pm\sqrt{2 \cdot \left(\frac{\Delta L}{N}\right)^2 + \left(\frac{L_{before} \cdot \Delta N}{N^2}\right)^2 + \left(\frac{L_{after} \cdot \Delta N}{N^2}\right)^2} \tag{4.3}$$

The error for ΔL is estimated to be $\Delta L = 0.25\mu m$, which comes from measurements of the SEM images in section 4.3 while the error for the number of ignitions ΔN depends on the on the total number of ignitions, as shown in table 4.1. The error is estimated to be higher for

Table 4.1: Errors for the number of ignitions

Time [min]	Ignitions N	Δt [s]	ΔN
2	1800	2	30
15	13500	10	150
30	27000	15	225
120	108000	180	2700
180	162000	300	4500

longer periods of time because of the possibility, that the plasma did not ignite because of a short circuit between the cables that go to the electrodes. In figure 4.4, ICCD images are shown of the treatment of a tungsten electrode with +20 kV at 15 Hz for 3 h.

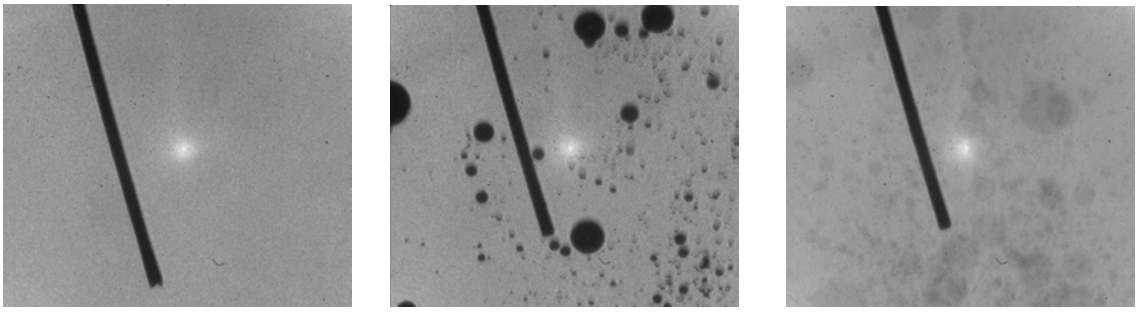

(a) (b) (c)

Figure 4.4: ICCD images of a tungsten electrode treated with +20 kV at 15 Hz. Figure (a) shows the electrode before treatment, (b) after 2 h 30 min using only a single scan and (c) after 3 h as 10 accumulated images. In (b) especially, the air bubbles are visible.

The material loss is clearly visible. What also is already visible from the ICCD images is the change of the shape of the electrode tip. Before the plasma treatment, the electrode tip has a pointed or bevelled, sharp shape due to the method of preparation. The tip is cut at a 45° angle, as can be seen in figure 4.10. The longer the treatment time, the more the

shape changes into something more flattened or round. The erosion rate for this particular configuration and also for the case of negative polarity is shown time resolved in figure 4.5.
What is already visible from figure 4.5 that at the beginning of the treatment, the erosion

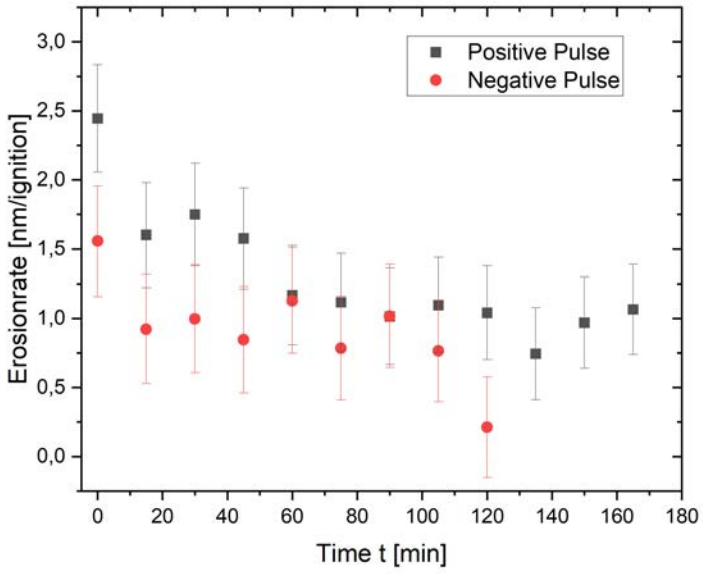

Figure 4.5: Time resolved erosion rate for tungsten electrodes treated with ±20 kV at 15 Hz. An image was taken every 15 min and the erosion rate was calculated between those points. The treatment time was 3 h for positive and 2 h for negative polarity.

rate is clearly higher than after a longer period of treatment. This is connected to the ignition mechanisms and especially the electric fields at the electrode tips. In figure 4.5 the measurement with 20 kV for negative polarity is also shown, but only for a treatment time of 2 h. There seems to be a difference in erosion rate due to the polarity of the pulse which can not be explained in a difference by dissipated energy, because as it was shown in figure 4.3, the dissipated energies for ±20 kV are nearly the same. The average erosion rates are shown in table 4.2 for both positive and negative polarity.

Table 4.2: Average erosion rates E_r for W treated with ±20 kV at 15 Hz.

Polarity of Pulse	$E_r / \frac{\text{nm}}{\text{ignition}}$	E_r without first data point / $\frac{\text{nm}}{\text{ignition}}$
+	1.23 ± 0.35	1.12 ± 0.35
-	0.91 ± 0.38	0.83 ± 0.38

There is an extra column for the erosion rates calculated without the first data point, because there is the greatest change in erosion rate. The explanation for this comes later. The time resolved erosion rate for platinum/iridium for positive and negative 20 kV is shown in figure 4.6. Whats already visible is that the positive erosion rates are clearly higher than the negative erosion rates. This is even more visible than for the tungsten case. The average erosion rates are shown in table 4.3 for both positive and negative polarity. Because of the fast change of the erosion rate in the first 30 min, measurements for the erosion rate were also done by taking images every 2 min for the first 30 min. The electric field is possibly higher at the

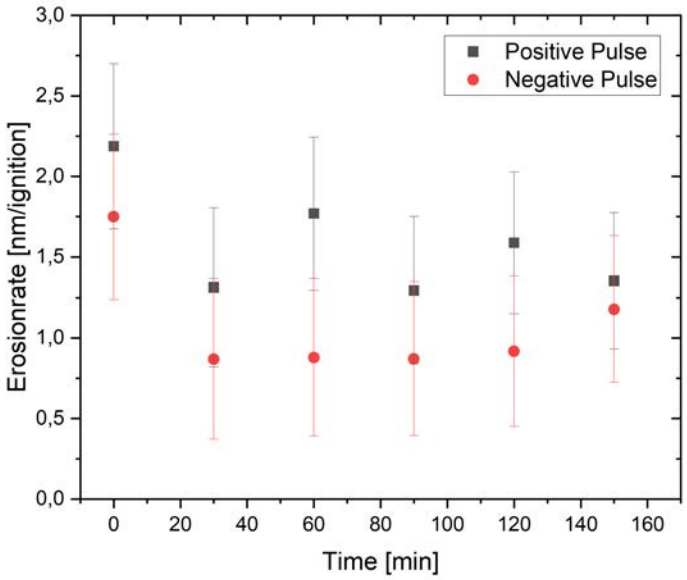

Figure 4.6: Time resolved erosion rate for a platinum/iridium electrode treated with ±20 kV at 15 Hz. An image was taken every 30 min and the erosion rate was calculated between those points.

Table 4.3: Average erosion rates E_r for Pt/Ir treated with ±20 kV at 15 Hz.

Polarity of Pulse	$E_r / \frac{\text{nm}}{\text{ignition}}$	E_r without first data point / $\frac{\text{nm}}{\text{ignition}}$
+	1.58 ± 0.46	1.46 ± 0.46
-	1.08 ± 0.48	0.94 ± 0.48

pointy tip which gets lost very quickly, this was already observed with the ICCD images. The erosion rate is of course also higher, because with the pointy shape, there is less material that can be eroded, the electrode is obviously thinner than for the later in time more cylindrical case. With those measurements, it will be possible to see when the tip changes its shape. The results are displayed in figure 4.7 for both tungsten and platinum/iridium for both polarities, respectively. Again, the greatest change for the erosion rate is at the beginning for both tungsten and platinum/iridium. Over the course of treatment, the erosion rate nearly reaches a plateau. What can also be extracted from those graphs are comparisons between the erosion rates of positive and negative pulses for each material, as has been done in table 4.4.

By taking the average erosion rates for all data points for the 30min, opposite trends are

Table 4.4: Average erosion rates E_r for W treated with ±24 kV and Pt/Ir treated with ±20 kV for 30 min, both at 15 Hz.

Material	Polarity of Pulse	$E_r / \frac{\text{nm}}{\text{ignition}}$	E_r without first data point / $\frac{\text{nm}}{\text{ignition}}$
W	+	3.53 ± 0.86	2.68 ± 0.86
W	-	4.06 ± 0.84	2.68 ± 0.84
PtIr	+	3.32 ± 0.72	2.61 ± 0.72
PtIr	-	2.02 ± 0.78	1.62 ± 0.78

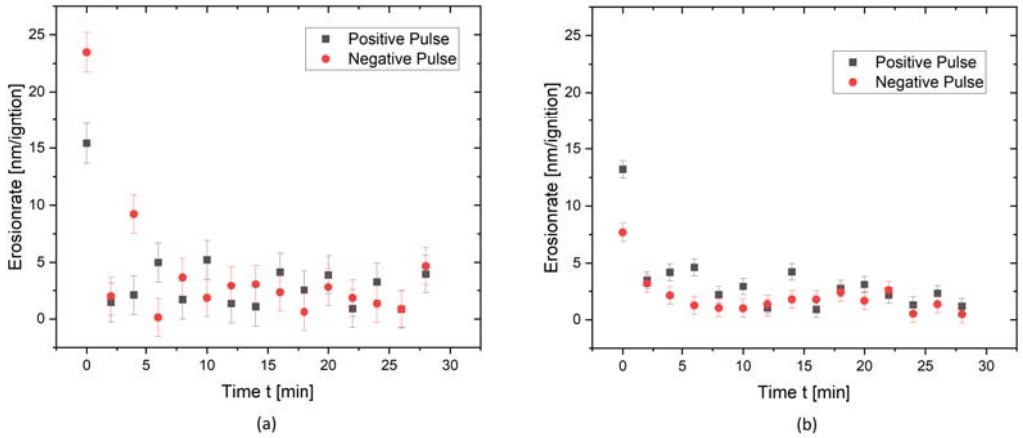

Figure 4.7: Time resolved erosion rates at 15 Hz for (a) tungsten electrodes with ±24 kV and (b) platinum/iridium electrodes with ±20 kV, both treated for 30 min.

recognisable. For tungsten, the negative pulses seem to have eroded more material while for platinum/iridium, the positive pulses resulted in a greater erosion rate. This is however with considering the first two minutes, were for negative-treated tungsten the erosion is way higher in the first two minutes than for positive pulses. The preparation of the electrode was rather uneasy and not exactly reproducible. It is possible that the electrode wire was cut in a way that lead to a greater erosion in this particular case.

A simple model can now be constructed to explain this behaviour for the first 30 min. The idea is, that the temperature T, that is responsible for the erosion rate, is proportional to the power

$$P = j \cdot E \propto T \tag{4.4}$$

Here, j is the current density. For the electric field E, we have equation 2.1:

$$E = \frac{U}{5 \cdot r_{\mathrm{E}}} \tag{4.5}$$

It is now possible to combine these equations and get:

$$T \propto \frac{U}{r_{\mathrm{E}}} \tag{4.6}$$

As later confirmed by the SEM images, the electrode is sharp or pointy at the beginning, resulting in a smaller radius of the electrode tip r_{E} which then leads, according to 4.6, to a higher temperature. The temperature T is then assumed to be also proportional to the erosion rate E_r, and with that, we can fit a function to the obtained erosion rates for the first 30 min, as done in figure 4.8. The x-axis was shifted by one minute in order to also account for the first data point with a fit function

$$y = \frac{A}{x} + B. \tag{4.7}$$

The physical meaning of y is the erosion rate, while B is the y intercept or point, at which erosion actually starts to happen. The factor A is the factor connecting the radius of the electrode tip to the erosion rate, in units: $\frac{\mathrm{nm} \cdot \mu\mathrm{m}}{\mathrm{ignition}}$. Obviously, this model is not good for

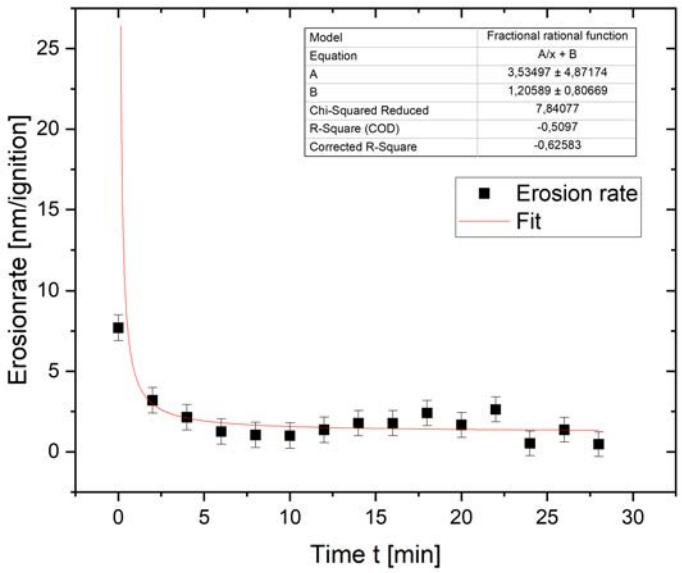

Figure 4.8: Erosion rate for platinum/iridium with -20 kV treated at 15 Hz for the first 30 min with pictures taken every two minutes. Additionally, the model fit was added.

predictions, as the error for the amplitude A is higher than the actual value and the corrected R-Square value is below 0. Nevertheless the function matches with the measurement points pretty accurately and for a first order approximation, seems to fit well.

Measurements were also done to determine the impact of the used voltage for the erosion rate, to find the impact of the voltage on the nanoparticle production. For that, only before and after treatment images were taken. Results for tungsten are shown in figures 4.9. In figure 4.9, a trend can be made out: the erosion rate is generally higher for a higher voltage, this goes for both positive and negative polarity. The average erosion rates are shown in table 4.5. This trend can also be made out for the platinum/iridium electrodes, also shown in figure 4.9.

Table 4.5: Average erosion rates E_r for W and PtIr treated with different voltages.

Material	Polarity of Pulse	$E_r / \frac{\text{nm}}{\text{ignition}} / \frac{\text{nm}}{\text{ignition}}$
W	+	0.97 ± 0.29
W	-	0.64 ± 0.32
PtIr	+	1.96 ± 0.3
PtIr	-	1.23 ± 0.46

Again, there is a difference between positive and negative polarity for the erosion rate, the positive polarity having clearly a higher erosion rate. It seems that the shape of the electrode tip significantly influences the erosion rates. The filigree assembly of the electrodes was not really reproducible, which could explain the outliers, e.g. the 20 kV erosion rate for negative pulses with a tungsten electrode, as shown in figure 4.2. It seems that the average erosion rate for platinum/iridium in dependence of the voltage is higher than for tungsten. This could come from the fact that the used alloy has a way lower melting point, between 1830° C and

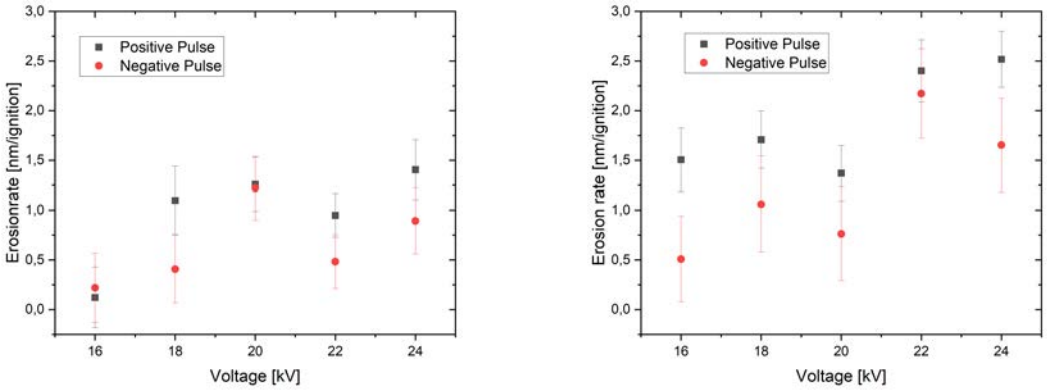

(a) Positive pulses (b) Negative pulses

Figure 4.9: Erosion rates depending on the used voltage for (a) tungsten and (b) platinum/iridium electrodes. The treatment time is 3 h, only for negative pulses for platinum/iridium it was 2 h.

2120° C, than tungsten, which has a melting point of 3410° C, both values according to the manufacturer. The conclusion could be that for a higher melting point, more energy must be dissipated to erode the same amount of material than for a for a lower melting point.
The obtained erosion rates can be again compared to Grosse [21]. Grosse measured an erosion rate of 0.94 mm/h or 17.41 $\frac{\text{nm}}{\text{ignition}}$ which is one magnitude higher than the measured erosion rates in this thesis. In [21], there was only one measurement provided for the erosion rate. It is quite possible that, because of an inconvenient angle of the wire compared to the ICCD camera, the erosion rate was estimated to be higher than the actual erosion rate. This is supported by the facts that within this thesis more measurements were carried out and that the erosion was not visible with the naked eye, while one millimeter per hour would have been already visible at treatment times of two or three hours.

It is now clear that the shape of the electrode changes dramatically with treatment, but the erosion reaches a plateau after some treatment. SEM images of the electrode tip can now provide additional information to explain this behaviour.

4.3 SEM Images

In the section before, the width of the electrode was just accepted to be the 50 μm stated by the manufacturer. This can now be verified. Additionally, the behaviour of the erosion rates in time can be explained further.
The SEM images confirm the stated widths of 50 μm by the manufacturer for the tungsten and platinum/iridium wire, as can be seen in figure 4.10. The cutting edge is clearly visible

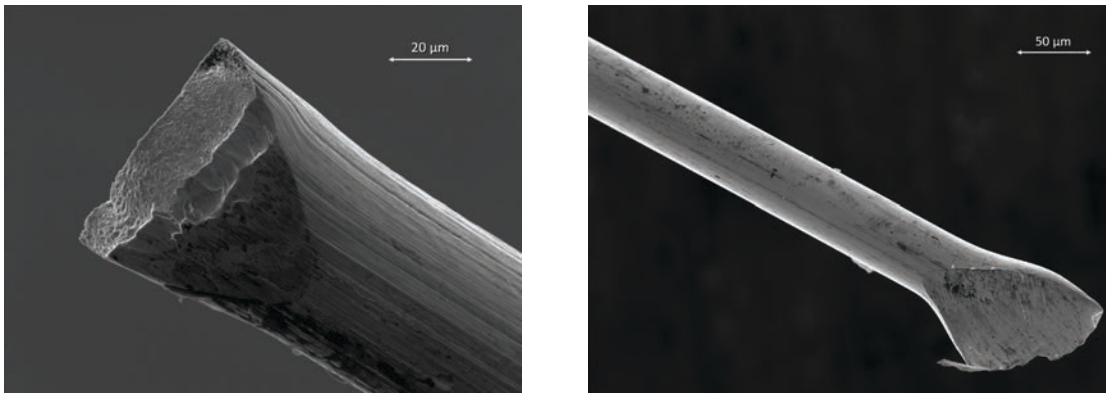

(a) (b)

Figure 4.10: SEM images of untreated electrode wires of (a) tungsten and (b) platinum/iridium alloy.

and sharper for the more temper tungsten, while for the platinum/iridium wire it seems smoother. The shape of the tip is important, because the greatest change of the erosion rate happens at the beginning, due to the higher electric field because of the smaller area. In order to get a rough understanding of the electric field around the electrode tip, a simple COMSOL multiphysics simulation [35] was done by Elia Jüngling to compare a sharp electrode and a semi-spherical electrode. This can be seen in figure 4.11. The voltage is 20 kV. The electric field strengths lie for both cases in the order of $10^8 \frac{\mathrm{V}}{m}$. From the theoretical background, the estimation is $1.6 \cdot 10^8 \frac{\mathrm{V}}{m}$ from equation 2.1 and $2.1 \cdot 10^8 \frac{\mathrm{V}}{m}$ from equation 2.2. The highest field strengths for the sharp electrode are only reached at the bottom and do not reach the side of the electrode, while for the round shape the highest field strengths go higher to the side, as can be seen by the red area with the highest field strength. The probability for the plasma to ignite is highest at the location of the highest field strengths and when the threshold, discussed in section 2.1.3, is reached. So the plasma ignites for the sharp electrode more often at the tip and this leads to a higher erosion rate which explains the within this thesis always observed higher erosion rate at the beginning of the measurement. The sharp shape of the electrodes vanishes after several minutes of treatment and leads to a more semi-spherical shape of the tip, as can be seen in figure 4.12. The shape of the tip in figure 4.12 is nearly semi-spherical. The diameter of this particular tip is roughly $d = (47.6 \pm 0.25)$ μm which leads to a radius of $r = (23.8 \pm 0.25)$ μm of a perfect sphere. The radius of the semi-spherical tip is approximately $r_T = (23.33 \pm 0.25)$ μm, which is a deviation of 2%. This is in favour that the plasma ignition reaches an equilibrium and evenly distributes on the surface of the electrode tip.
Other treated electrodes can be found in figure 4.13.

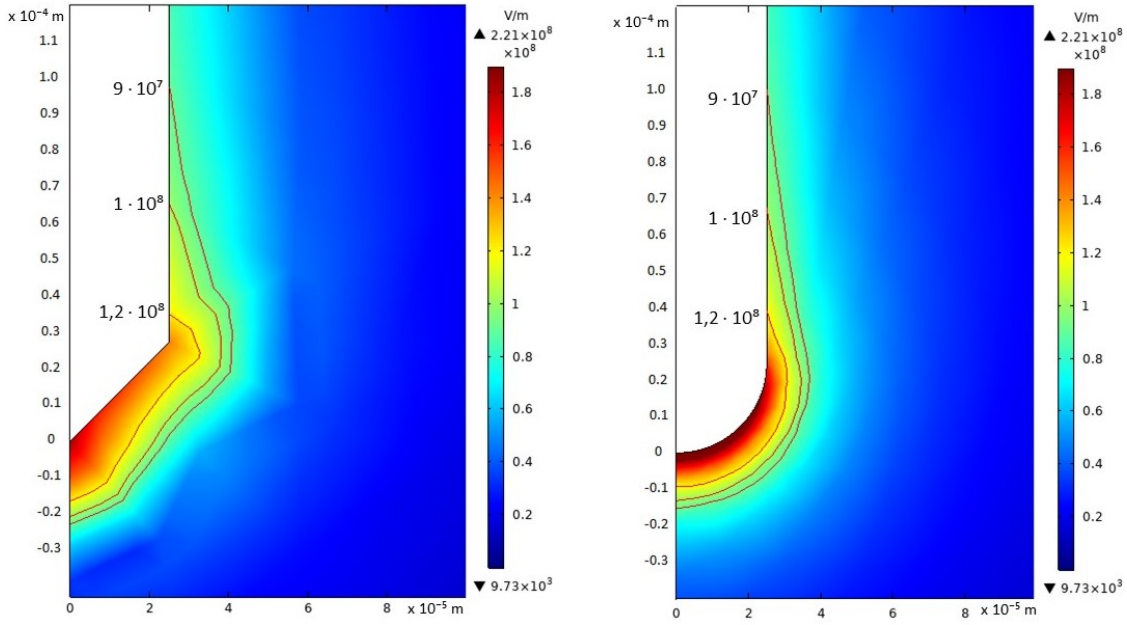

(a) (b)

Figure 4.11: Electric field strengths simulated for the setup used in this thesis using COMSOL multiphysics [35], done by Elia Jüngling.

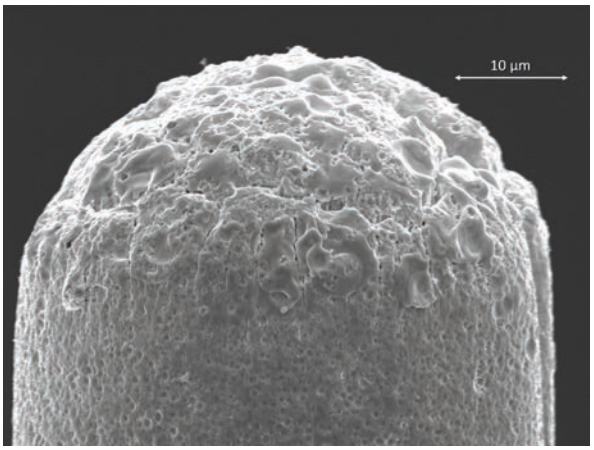

Figure 4.12: SEM Image of an treated tungsten electrode. The treatment time was 3 h at +20 kV with 15 Hz.

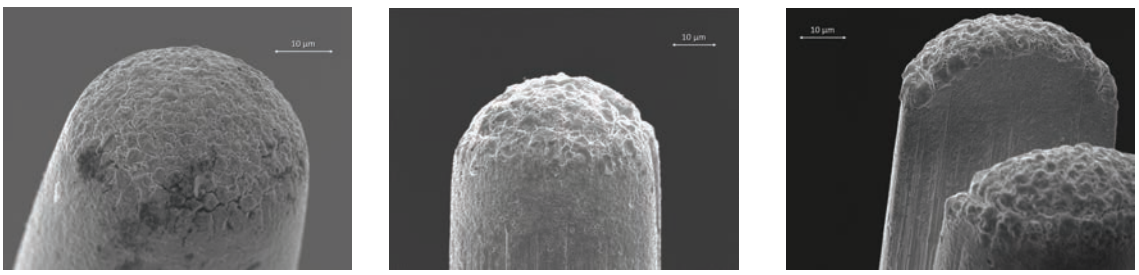

(a) (b) (c)

Figure 4.13: Images of different treated tungsten electrodes. The treatment time was for all three electrodes 3 h, (a) is with +16 kV, (b) with +20 kV and (c) with +24 kV. The +24 kV electrode happened to split up at the top.

Different surface structures for different voltages are visible in figure 4.13. The treated electrodes show trenches or crevices that make the surface look really ruptured. It is possible that these lie at the points which come from the production of the wires, where the metal fibre gets elongated. For higher voltages, in the case of the tungsten electrodes, treated with positive polarity, the hills in between the crevices seem to gain in height.
The 24 kV treated tungsten electrode happened to split up from the top down the wire and with that gives the possibility to look how deep the melting and solidification go into the electrode. The depth of this is around $(5.4 \pm 0.35)\ \mu m$.
A measurement with only 25 plasma ignitions for a platinum/iridium electrode was performed and can be seen in figure 4.14.

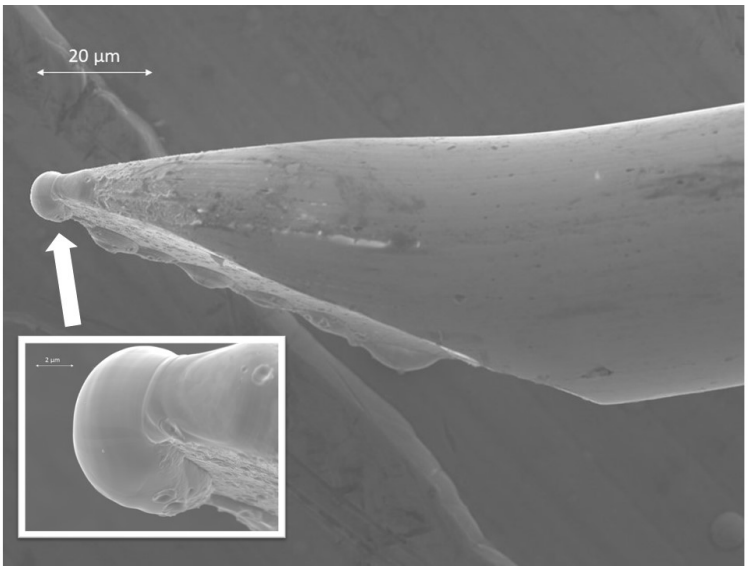

Figure 4.14: SEM Image of an treated platinum/iridium electrode. The plasma was ignited 25 times using this electrode with +20 kV at 1 Hz. Melted bubbles can be distinguished, especially the one zoomed in at the tip.

The surface on the side is still smooth as seen on untreated electrodes, while on the tip bubble-like structures have formed to the cutting point. A possible explanation would be that those melting points are caused by the plasma itself. There are not 25 of those bubbles visible, but because of the unfortunate placement of the electrode tip, there could be more than the visible approximated 8-10. It is also possible that the plasma ignited at the sharpest point of the tip multiple times, which is probable because of the high electric field there. The crevices for longer treatment times seen in other electrodes are not visible.
In figure 4.15 negatively treated tungsten electrodes are shown. The difference to the positive ones is clearly visible. Here, the all three electrodes happened to split up. How deep the melting and solidification goes is not clearly visible for the -20 kV and -24 kV case, but for the -16 kV case it is roughly $\approx (6.3 \pm 0.4)\ \mu m$, which is higher than the positive case with a higher voltage of 24kV, which had a depth of $(5.4\pm 0.35)\ \mu m$. The images from the other electrodes however indicate that the deepness becomes smaller, possibly because there is more erosion. The -20 kV and -24 kV electrode do not have a smooth surface like their positive counterparts and the shape of the tip is not really round. Also there are some black spots which could originate from the plasma, already came with the wire or are from some glue that held the wire on its roll.
Figure 4.16 shows SEM images of platinum/iridium electrodes treated with positive pulses

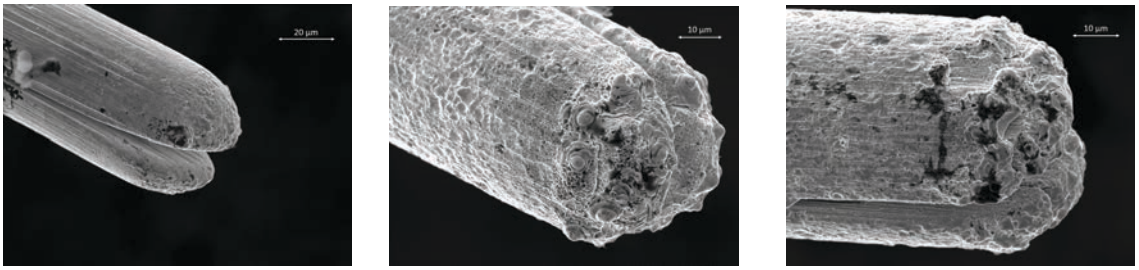

(a) (b) (c)

Figure 4.15: Images of different treated tungsten electrodes. The treatment time is for all three electrodes 3 h at 15 Hz, (a) is with -16 kV, (b) with -20 kV and (c) with -24 kV. All three electrodes happened to split up.

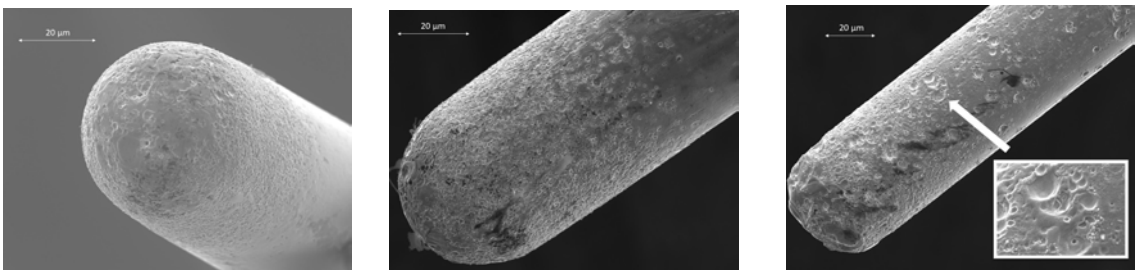

(a) (b) (c)

Figure 4.16: Images of different treated platinum/iridium electrodes. The treatment time is for all three electrodes 3 h at 15 Hz, (a) is with +16 kV, (b) with +18 kV and (c) with +24 kV.

with different voltages while figure 4.17 shows the treated electrodes with negative polarity. The tip of the electrodes treated with ±16 kV look similar, and even higher up the surface structure is the same, having a clear border between treated and untreated surface. Only the contrast with which the images were taken makes the negatively treated one look more dark. For both cases there are some bigger melted spots directly on the tip and many small craters having a size of $\approx 1\ \mu m$. Also the tip has a clear semi-spherical shape.
For the electrodes treated with 18 kV and 20 kV with positive and negative polarity, respectively, the melted areas get bigger. Now there are more craters for the positive treated one than for the negative treated one and the one treated with positive polarity has a more semi-spherical shape at the tip then the negative one, which shows more ruptures. Also on the positive one, there are some small dark points which could come again from the glue of the wire or have some other origin, while the negative one does not show this.
The shape of the tip changes dramatically for the ±24 kV treated electrodes. It is nowhere near as semi-spherical and both show less craters than the 18 kV and 20 kV electrodes. In contrast between the two 24 kV electrodes, there are more bigger irregular craters with diameters of $\approx 5\ \mu m$ for the positive one than for the negative electrode. For both, there are even some relatively deep holes of maybe $\approx 0.5\ \mu m$ depth. The ignition takes now place on the whole electrode and not just the tip, there is not a clear border between where the ignition happens and where it does not, it is now more transitional. All those differences between the tungsten and platinum/iridium electrode could possibly be explained by the different melting points, which are for tungsten 3410° C and for the platinum/iridium alloy between 1830° C and 2120° C, as stated by the manufacturer Goodfellow Cambridge Ltd.

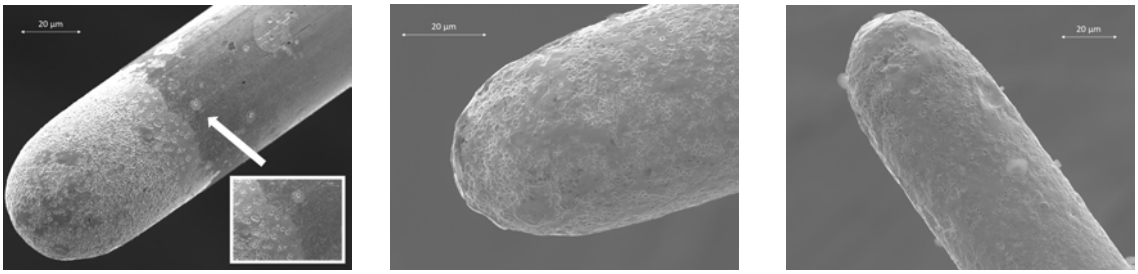

(a) (b) (c)

Figure 4.17: Images of different treated platinum/iridium electrodes. The treatment time is for all three electrodes 2 h at 15 Hz, (a) is with -16 kV, (b) with -20 kV and (c) with -24 kV.

To draw a conclusion, it was observed that for smaller voltages, the erosion rate is lower and the electrode is eroded in a evenly distributed way. For higher voltages, the erosion seems to happen more abrupt, leading to bigger craters and not to an approximately semi-spherical tip, especially for the negative polarity case. Comparing the SEM images to the ones made by Lukeš et al. [16], there are some differences visible. First of, although stated that they used also used needle electrodes, the SEM images show that the tips have way more of a cone shape. The craters, especially for the lower voltages, are comparable, but for higher voltages the observed surface structures in this thesis differ clearly from the ones presented by Lukeš et al., especially for tungsten, showing even growing structures. Unfortunately, they only took the SEM images for the positive polarity.

Now, with the knowledge of the erosion and the different surface structures, it is suitable to take a look at the plasma-assisted produced nanoparticles with TEM images.

4.4 TEM Images

The next section is about the images of the produced nanoparticles using a TEM. The obtained distilled water samples with nanoparticles have been prepared for TEM analysis the way described in section 3.2. The following figure 4.18 shows images of a sample that has been produced by a tungsten electrode operated with 24 kV at 15 Hz for 3 h with positive polarity.

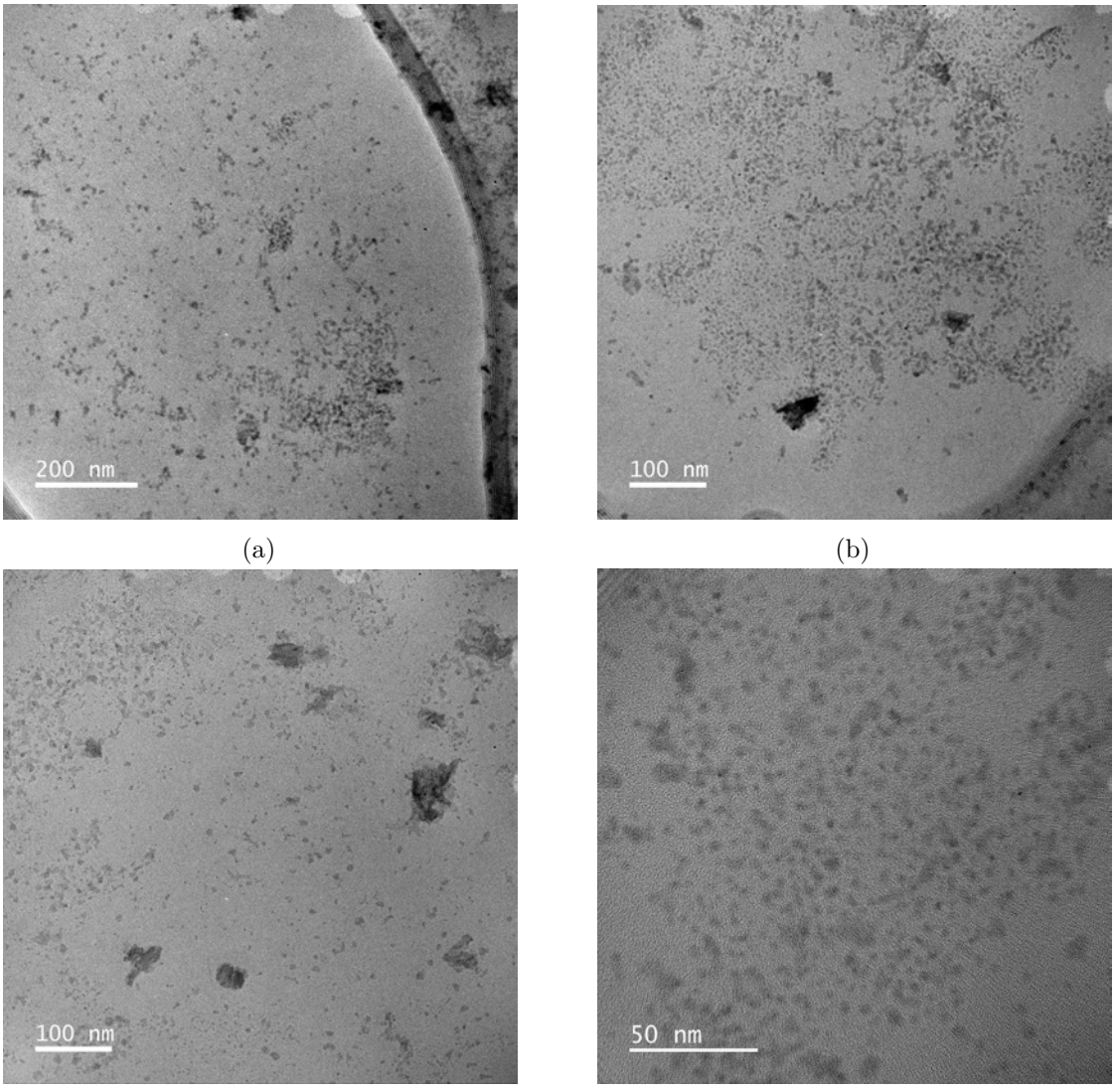

(a) (b)

(c) (d)

Figure 4.18: (a)-(d): A sample with nanoparticles produced with a tungsten electrode with +24 kV at 15 Hz for 3 h in different resolutions. There are large amounts of small nanoparticles in the range of ≈ 5 nm.

There are a lot of small nanoparticles roughly the size of ≈ 5 nm more or less evenly distributed in the sample with small clusters. The line seen in figure 4.18 comes from the preparation of the sample and is the thin carbon film. This case looks a lot better than the case for -24 kV treated tungsten electrode at 15 Hz for 3 h, shown in figure 4.19. In this sample, the concentration of nanoparticles is very low. There are only a few clusters of nanoparticles with sizes over 100 nm and small spherical nanoparticles with sizes ≈ 25 nm. It is generally hard

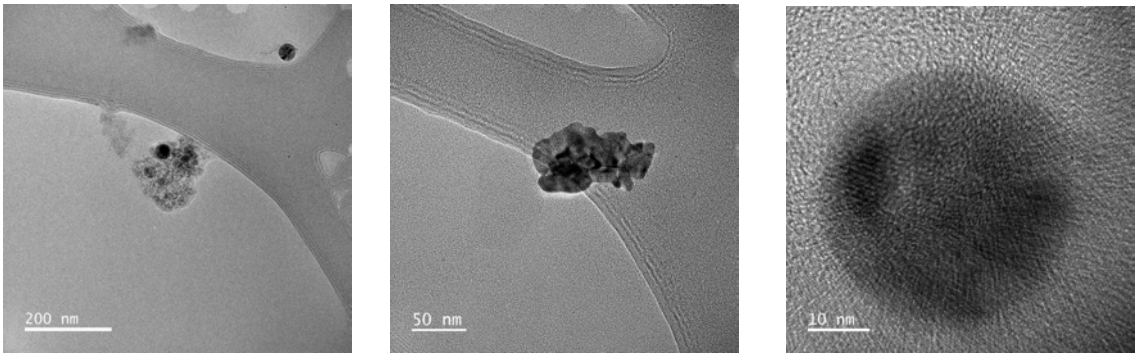

(a) (b) (c)

Figure 4.19: (a)-(c): A sample with nanoparticles produced with a tungsten electrode with -24 kV at 15 Hz for 3 h with a negative polarity.

to make a statement about the total number of nanoparticles and in contrast to the +24 kV treated electrode, there is a only a fraction of nanoparticles. Unfortunately, the TEM was out of order for additional measurements with platinum/iridium nanoparticles.
Now with the knowledge of how big the nanoparticles are, another interesting calculation is for the number of tungsten atoms being removed from the electrode in order to estimate the number of the nanoparticles. The atomic structure for tungsten is body-centered cubic and the edge length is $d = 0.316$ nm [36]. The electrode wire is approximated as a cylinder, so one atomic plane has the area of

$$A = \pi r^2 = \pi \cdot \left(\frac{50\,\mu\text{m}}{2}\right)^2 = 1.96 \cdot 10^{-9}\,\text{m}^2 \tag{4.8}$$

The number of atoms in one atomic plane is then:

$$\frac{A}{d^2} = \frac{1.96 \cdot 10^{-9}\,\text{m}^2}{(0.316 \cdot 10^{-9}\,\text{m})^2} = 1.96 \cdot 10^{10}\,\text{Atoms} \tag{4.9}$$

With an erosion rate of e.g. 1,26 $\frac{\text{nm}}{\text{ignition}}$ for a positive 20 kV pulse and a distance between atomic layers of $0.5 \cdot 0.316$ nm, the number of removed atoms per ignition is:

$$1.96 \cdot 10^{10}\,\text{Atoms} \cdot \frac{1.26\,\frac{\text{nm}}{\text{ignition}}}{0.5 \cdot 0.316 \cdot 10^{-9}\,\text{m}} = 1.57 \cdot 10^{11}\,\frac{\text{Atoms}}{\text{ignition}} \tag{4.10}$$

We can now calculate, how many atoms are in one nanoparticle. For that, we use that in a unit cell of tungsten, there are five atoms (body-centered cubic). The edge length is 0.316 nm and with that, we obtain:

$$N = 5 \cdot \frac{\frac{4}{3}\pi \cdot (2.5\,\text{nm})^3}{(0.316\,\text{nm})^3} \approx 10000 \tag{4.11}$$

So, assuming that every atom goes into a nanoparticle with a diameter of 5 nm, we should obtain roughly 15 million nanoparticles per ignition. This is obviously not the case, a lot of atoms go into the distilled water, or solidify at the surface again and stay attached to the rest of the electrode.

In the next section, the laser ablation process in comparison to the plasma-assisted process of nanoparticle production will be discussed.

4.5 Laser Ablation

As a comparison to the plasma-assisted nanoparticle production, the production via laser ablation was performed. Unfortunately, the setup used at Lidtrotec GmbH has a working volume with distilled water of 2 l which is, for the TEM analysis, way too much water and the nanoparticles would be very diluted. The production of nanoparticles in literature leads to very different particle sizes, depending on target material, wave length of the laser, deposited energy and more. Nanoparticles in a comparable size to the ones observed in this thesis with diameters of around 5 nm have also been found [37].
It was however possible to obtain SEM images of the surfaces of the target materials. Additional measurements where made with the correct settings and single bursts. The treatment time was then 3 min with 15 Hz with the average power of 440 mW and deposited energy of 3,07 J and for 15 min with the same values. The untreated surfaces can be seen in figure 4.20. The platinum/iridium foil was generally more smooth and did not have many surface

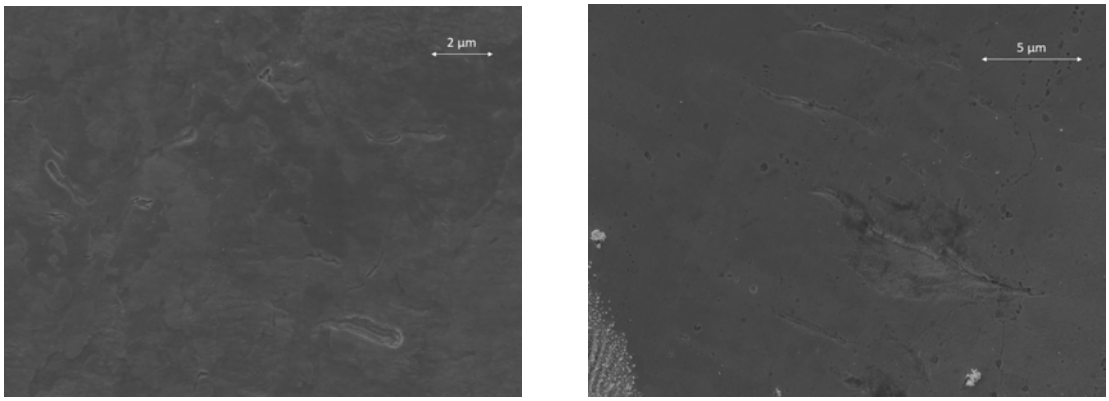

(a) (b)

Figure 4.20: Untreated surface of the (a) tungsten foil and (b) platinum/iridium foil. In (b) in the bottom left corner, there is already the border to the crater visible

characteristics, while the tungsten foil had many irregularities. The treated surfaces for both tungsten and platinum/iridium for 3 min and 15 min can be seen in figure 4.21. The craters show some peculiar characteristics. First of, it was not possible to look at the bottom of the craters with the SEM. The laser beam had a diameter of roughly 10 μm and the craters have an even bigger diameter, which comes from the fact that the laser is not accurate down to the μm scale. The case for only 3 min treatment time of the tungsten foil shows some direct ruptures around it that look layered. The 15 min treatment time does not show this for tungsten on every side, only a small edge is visible on the left, however the surface that goes into the crater, shown in figure 4.22 is the same on the outside. The surface structure in the crater seems to be similar for both cases. The crater for 15 min treatment time also is significantly bigger and seemingly also deeper than for the shorter treatment time. The platinum/iridium craters show some different characteristics in contrast to the tungsten case: small cluster of platinum/iridium particles with diameters below 1 μm have been made by the laser ablation process. They show especially at uneven points on the surface, possibly attaching to it after being transported by the flowing water. There is a wave-like structure all around the crater, probably coming from the flowing water. Here, the crater for the longer treatment time is also bigger and it even seems like deeper than the case for the shorter treatment time. While for the tungsten shape, the small peaks point into the crater all around it, there are no visible peaks for the platinum/iridium case. However, there is the wave like

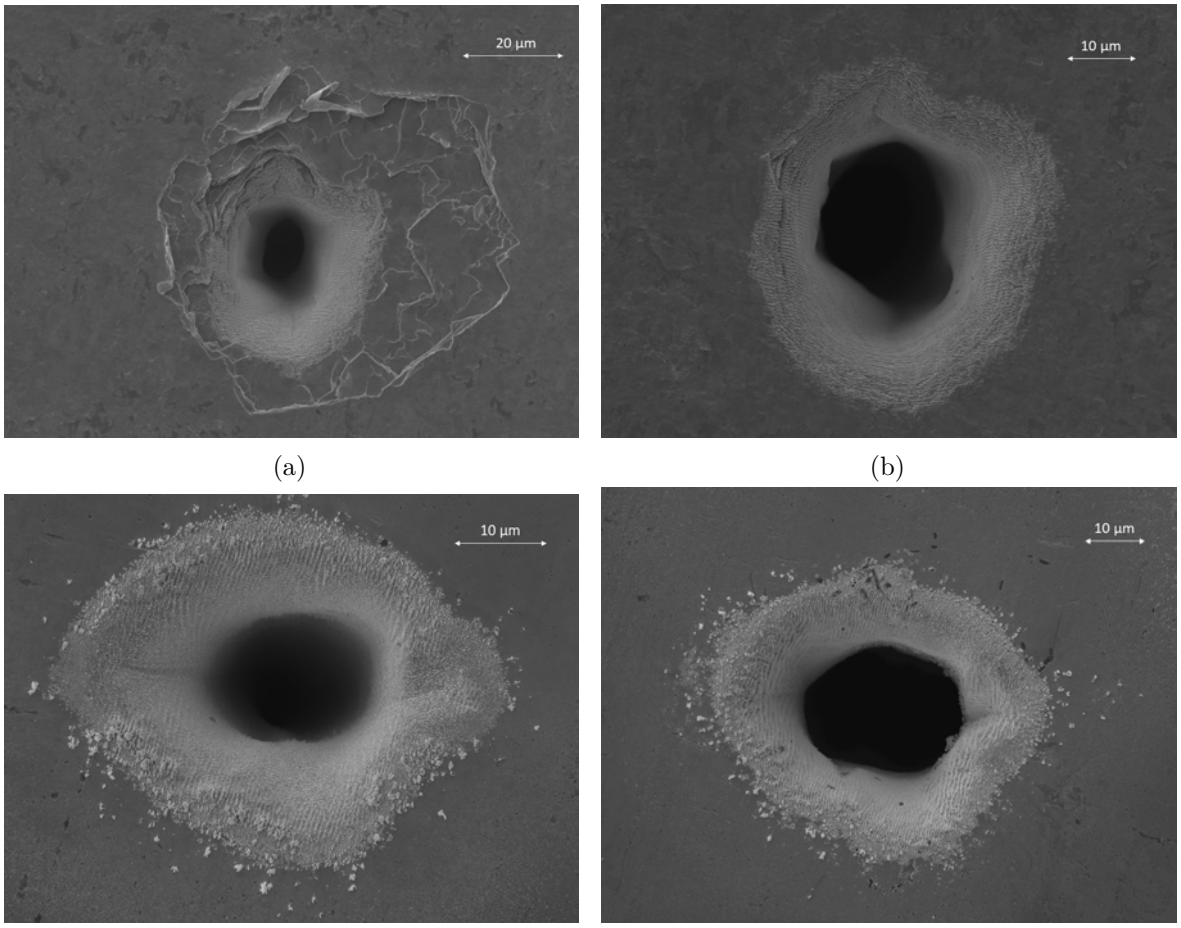

Figure 4.21: SEM images of the craters made by laser ablation. Images (a) and (b) show the tungsten foil treated for 3 min and 15 min, respectively, while images (c) and (d) show the platinum/iridium foil treated for also 3 min and 15 min, respectively.

structure. This difference in shape probably comes from the different melting points of the materials, which are the same as for the electrodes, namely 3410° C for tungsten and between 1830° C and 2120° C for platinum/iridium, stated by the manufacturer Goodfellow Cambridge Ltd.
As a comparison to the surfaces of the electrodes 4.3, there are some similarities. The small craters at the electrode surfaces, especially observed for the lower voltages for both materials like in figure 4.17, also appear on the surfaces around the craters, however in relatively low quantities in comparison to the electrodes. This may favor the interpretation that the plasma can ignite at several places around the electrode, while for the laser ablation case, it ignites on the surface, digging into the hole and creating the crater, and does not reach the outer border that often, where the small craters appear and stay, due to the fact that there is not much material ablated.
As already mentioned, it was unfortunately not possible to make TEM images of the produced nanoparticles. However, by judgement of the eye, it is probably the case that for those short treatment times, the plasma-assisted process was more efficient, due to the fact that the crater is smaller in dimension in comparison the the electrode.

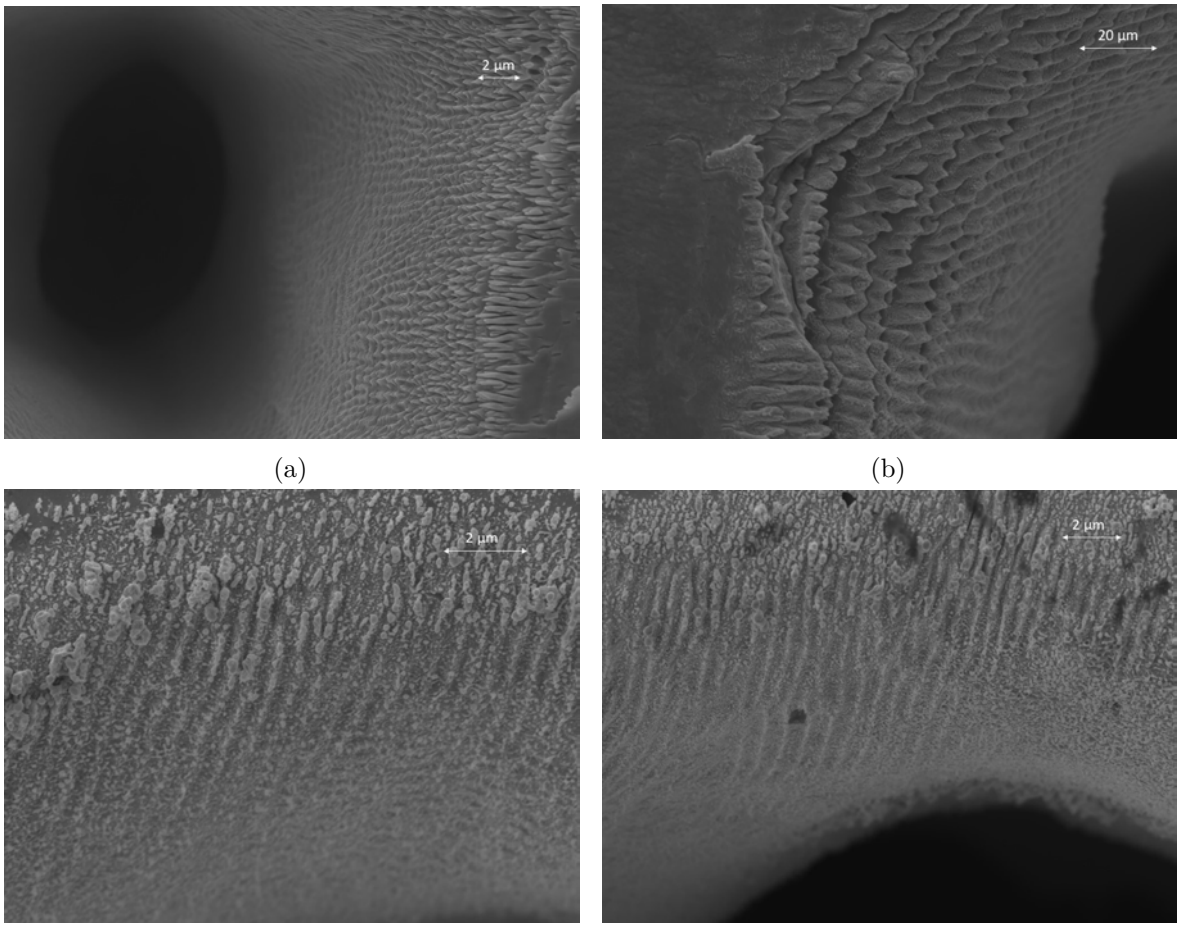

(a) (b)

(c) (d)

Figure 4.22: SEM images of the crater edges made by laser ablation. Images (a) and (b) show the tungsten foil treated for 3 min and 15 min, respectively, while images (c) and (d) show the platinum/iridium foil treated for also 3 min and 15 min, respectively.

5 Conclusion and outlook

In this thesis, the plasma-assisted nanoparticle production was investigated via the measurement of the erosion of the electrodes. This was done using ICCD images to measure the length of the electrode wire before and after treatment with the nanosecond pulsed plasma. Additional measurements were for the dissipated power and energy as well as images obtained by SEM for the electrode wires and TEM images for the produced nanoparticles.

The dissipated energies are consistent with literature and lie in the range of tens of mJ per pulse. It is however possible that this value may not be accurate, because of the length of the cable and possible internal power losses, due to the fact that the used cable is self made. The trend, that for higher voltages the dissipated powers and energies are higher, seems appropriate.
The measured erosion rates are in the range of a few nanometers per ignition. A great change in erosion rate over time is seen especially at the beginning of treatment, where the erosion rate could be even ten times higher than for a later point in time. This has been attributed to be an effect of the higher electric field at the tip of the sharp electrode at the beginning, before erosion took place. Additionally, the cylindrical approximation for the wire is not true, the way of cutting usually lead to a more pointy-shaped tip. What was also observed is that the average erosion rate was going up for higher voltages thus higher dissipated energies, which also seems reasonable. The erosion rates for positive and negative polarity were often comparable, but the erosion rates for positive pulses were somewhat higher, which also can be explained with the circumstance that the positive pulses, especially for higher voltages, dissipated more energy. These conditions were observed for both the tungsten and the platinum/iridium electrodes. The comparison between both materials also seems to line up with the properties of the materials: tungsten, having a higher melting point, had lower erosion rates than the platinum/iridium alloy, which has a lower melting point. These observed erosion rates do not line up with previous measurements with this setup, nevertheless seem reasonable, as already discussed.
In order to understand what was happening to the electrodes during treatment, SEM images were taken, which will be discussed next. The SEM images confirm the sharp shape of the electrode at the beginning and also confirm the stated width of the electrode, used later as reference for all erosion rates. The electrodes after treatment exhibit different kind of surface structures for different treatment voltages. While for smaller voltages, the electrodes had many small craters that were distributed evenly around the tip and ended at a border, this definite structure was lost for higher voltages. The shapes of the electrode tips changed from sharp and pointy to semi-spherical. This was especially observed for relatively low voltages, for the higher voltages the semi-spherical shape became more irregular due to larger melting spots. Interestingly, an image for the first 25 plasma ignitions of a platinum/iridium electrode showed not really the beginning of the erosion process, but melted and solidified bubble-like structures of platinum/iridium alloy formed on the smooth surface of the sharp electrode. The observation, that the erosion happens at the highest point of the electric field and thus leading to a semi-spherical shape is reasonable and in accordance with literature.
Coming to the other electron microscope, the TEM, it showed images of the nanoparticles

themselves. Unfortunately, because of maintenance, unforeseen complications and repair works at the TEM, only images for the tungsten nanoparticles were able to be made. For the negative polarity case, only irregular and particles of many sizes could be observed. It was not possible to determine the chemical composition of them, for that, further analysis would be needed, for example with energy dispersive x-ray spectroscopy. For the case of positive polarity, a lot of evenly distributed nanoparticles have been observed. The sizes were also nearly the same at around 5 nm. For lower voltages, only very little nanoparticles could be found in the samples. This is also reasonable due to the fact that for higher voltages, higher erosion rates have been measured.
Summing up the last part of the results, the laser ablation, leads to some degree of dissatisfaction. It was certainly not possible to find nanoparticles for this short treatment times in 2 l of distilled water, and even if it was possible, this experiment only was done when the TEM was already in maintenance. However, SEM images of the used target foils were taken. They showed similarities and differences to the electrodes, made out of the same material. It was not possible to determine the depth of the crater, however the possibility is high that the plasma-assisted nanoparticle production was more efficient, judging by the fact that the diameter of the crater is approximately only half the diameter of the electrode. But without a depth of the crater, this can not be confirmed and remains speculation.
In conclusion, it can be said that this setup can have a high efficiency of nanoparticle production, but more measurements are definitely needed to compare it to other conventional ways of nanoparticle production.

As an outlook, what could be done in the future, there are many ideas. First of, it would be interesting to take images of the platinum/iridium nanoparticles, to check whether they have the same size distributions as the tungsten nanoparticles. Additionally, the chemical composition of the nanoparticles could be obtained with dispersive x-ray spectroscopy or dynamic light scattering (DLS). Furthermore, to gain a better understanding of what is happening at the ignition of the plasma at the electrode tip, an estimation of the temperature, for example via black-body-radiation. Erosion rates could also be measured for even higher voltages for this setup with the right precautions, for example testing if the electrode is melted or avoidance of other damage to the setup. Apart from this, there is a wide range of other possible materials for the electrodes, and it could be possible to produce nanoparticles consisting of other materials.

A Appendix

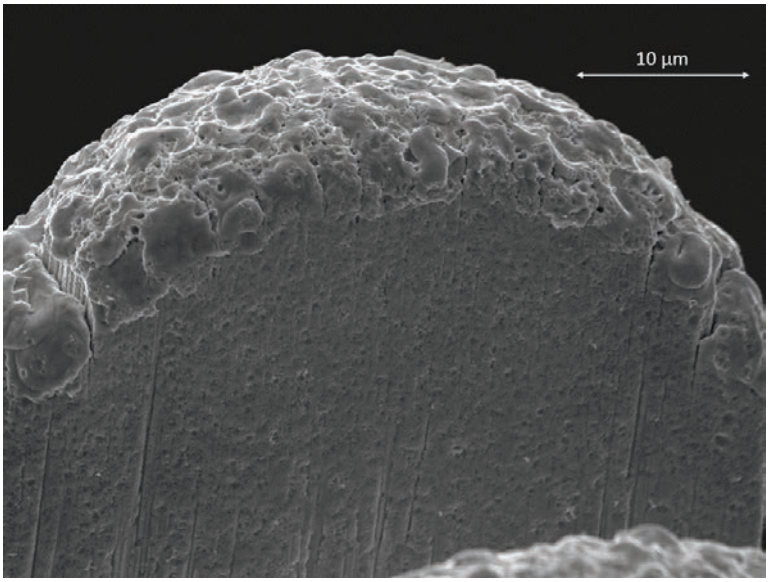

Figure A.1: SEM Image of a tungsten electrode treated with +24 kV at 15 Hz for 3 h. The electrode happened to split up, the fibres from the production process are visible.

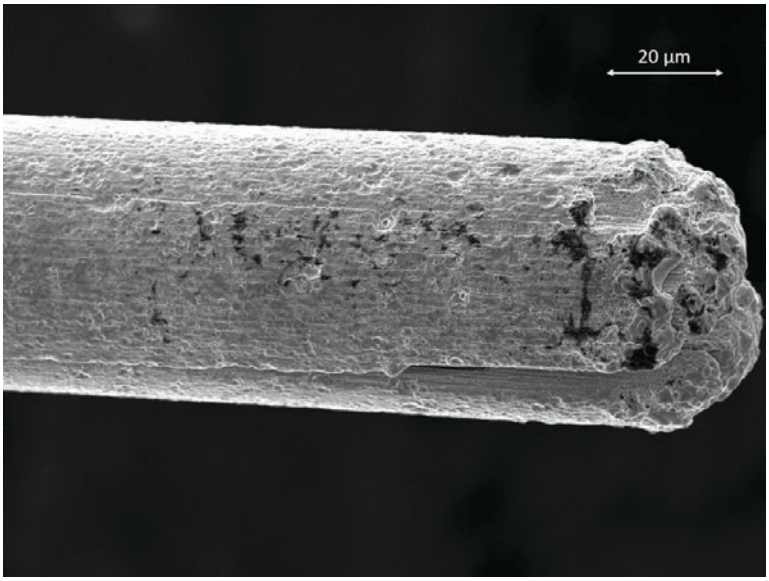

Figure A.2: SEM Image of a tungsten electrode treated with -24 kV at 15 Hz for 3 h. The electrode happened to split up, the fibres from the production process are visible. Also some kind of glue (black spots) are visible.

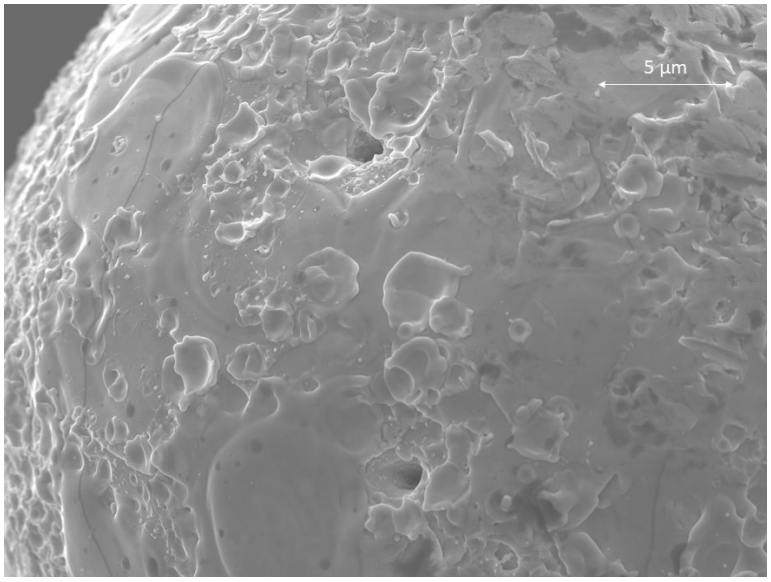

Figure A.3: SEM Image of a platinum/iridium electrode treated with +16 kV at 15 Hz for 3 h. Visible are some melted surfaces and two holes inside the electrode.

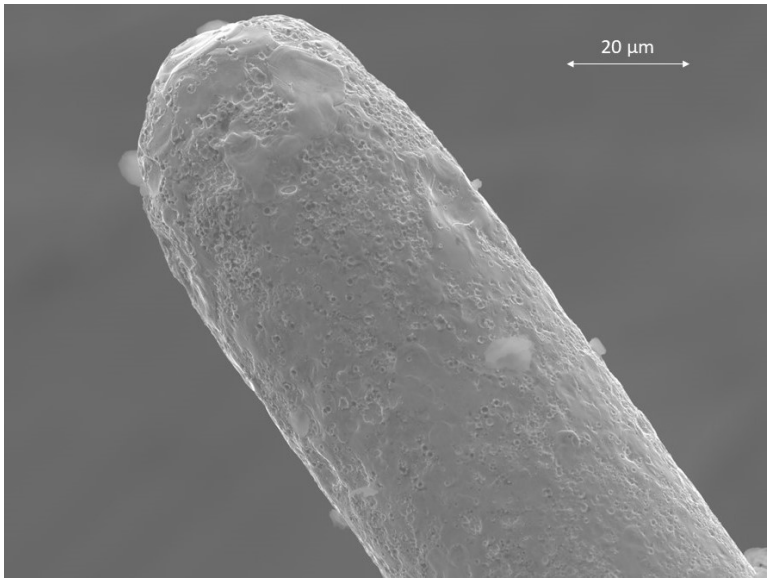

Figure A.4: SEM Image of a platinum/iridium electrode treated with -24 kV at 15 Hz for 2 h. Visible are some bigger melted surfaces.

Bibliography

[1] B. Jiang et al. "Review on electrical discharge plasma technology for wastewater remediation." In: *Chemical Engineering Journal* (2013). DOI: https://doi.org/10.1016/j.cej.2013.09.090 (cit. on pp. iii, iv, 1).

[2] M. Tichonovas et al. "Degradation of various textile dyes as wastewater pollutants under dielectric barrier discharge plasma treatment." In: *Chemical Engineering Journal* (2013). DOI: https://doi.org/10.1016/j.cej.2013.05.095 (cit. on pp. iii, iv, 1).

[3] A. V. Nominé et al. "Synthesis of nanomaterials by electrode erosion using discharges in liquids." In: *J. Appl. Phys. 130, 151101* (2021). DOI: https://doi.org/10.1063/5.0040587 (cit. on pp. iii, iv, 1, 4, 6, 8).

[4] S. A. Maier et al. "Plasmonics—A Route to Nanoscale Optical Devices." In: *Advanced Materials Volume 13, Issue 19* (2001). DOI: https://doi.org/10.1002/1521-4095(200110)13:19<1501::AID-ADMA1501>3.0.CO;2-Z (cit. on pp. iii, iv, 1).

[5] G. A. Martínez-Castañón et al. "Synthesis and antibacterial activity of silver nanoparticles with different sizes." In: *J. Nanopart. Res. 10, 1343–1348* (2008). DOI: https://doi.org/10.1007/s11051-008-9428-6 (cit. on pp. iii, iv, 1).

[6] H. Akiyama. "Streamer Discharges in Liquids and their Applications." In: *IEEE Transactions on Dielectrics and Electrical Insulation (Volume: 7, Issue: 5)* (2000). DOI: https://doi.org/10.1109/94.879360 (cit. on p. 1).

[7] J. L. West and N. J. Halas. "Engineered Nanomaterials for Biophotonics Applications: Improving Sensing, Imaging and Therapeutics." In: *Annu. Rev. Biomed. Eng.* (2003). DOI: https://doi.org/10.1146/annurev.bioeng.5.011303.120723 (cit. on p. 1).

[8] A. Henglein. "Colloidal Silver Nanoparticles: Photochemical Preparation and Interaction with O_2, CCl_4, and Some Metal Ions." In: *Chemistry of Materials* (1997). DOI: https://doi.org/10.1021/cm970613j (cit. on p. 1).

[9] J. Zhu et al. "Shape-Controlled Synthesis of Silver Nanoparticles by Pulse Sonoelectrochemical Method." In: *Langmuir 16, 16, 6396–6399* (2000). DOI: https://doi.org/10.1021/la991507u (cit. on p. 1).

[10] A. A. Ashkarran. "A novel method for synthesis of colloidal silver nanoparticles by arc discharge in liquid." In: *Current Applied Physics* (2010). DOI: https://doi.org/10.1016/j.cap.2010.05.010 (cit. on pp. 1, 7).

[11] F. Taccogna. "Nucleation and growth of nanoparticles in a plasma by laser ablation in liquid." In: *J. Plasma Phys.* (2015). DOI: https://doi.org/10.1017/S0022377815000793 (cit. on pp. 1, 8).

[12] P. Bruggeman and C. Leys. "Non-thermal plasmas in and in contact with liquids." In: *Journal of Physics D: Applied Physics 42.5* (2009). DOI: https://doi.org/10.1088/0022-3727/42/5/053001 (cit. on p. 3).

[13] P. J. Bruggeman et al. "Plasma–liquid interactions: a review and roadmap." In: *Plasma Sources Sci. Technol.* (2016). DOI: https://doi.org/10.1088/0963-0252/25/5/053002 (cit. on pp. 3, 4).

[14] N. Sano. "Formation of multi-shelled carbon nanoparticles by arc discharge in liquid benzene." In: *Materials Chemistry and Phyiscs* (2004). DOI: https://doi.org/10.1016/j.matchemphys.2004.07.018 (cit. on pp. 4, 7).

[15] K. Grosse et al. "Nanosecond pulsed discharges in distilled water: I. Continuum radiation and plasma ignition." In: *Plasma Sources Sci. Technol.* (2020). DOI: https://doi.org/10.1088/1361-6595/aba487 (cit. on p. 4).

[16] P. Lukeš et al. "Erosion of Needle Electrodes in Pulsed Corona Discharge in Water." In: *Czechoslovak Journal of Physics* (2006). DOI: https://doi.org/10.1007/s10582-006-0304-2 (cit. on pp. 4, 7, 28).

[17] R. Gomer. "Field Emission and Field Ionization in Condensed Phases." In: *Accounts of Chemical Research* (1971). DOI: https://doi.org/10.1021/ar50050a001 (cit. on pp. 4, 5).

[18] Y. Seepersad et al. "Investigation of positive and negative modes of nanosecond pulsed discharge in water and electrostriction model of initiation." In: *Journal of Physics D: Applied Physics* (2013). DOI: https://doi.org/10.1088/0022-3727/46/35/355201 (cit. on pp. 4, 6).

[19] S. M. Korobeinikov et al. "Breakdown Initiation in Water with the Aid of Bubbles." In: *High Temperature* (2002). DOI: https://doi.org/10.1023/A:1020420216579 (cit. on p. 4).

[20] K. Grosse et al. "Ignition and propagation of nanosecond pulsed plasmas in distilled water—Negative vs positive polarity applied to a pin electrode." In: *Journal of Applied Physics* (2021). DOI: https://doi.org/10.1063/5.0045697 (cit. on p. 4).

[21] K. Grosse. *Discharge ignition, dynamics and chemistry of nanosecond pulsed plasmas in water*. Dissertation. 2020 (cit. on pp. 4, 6, 12, 16, 17, 23).

[22] W. A. Schmidt. "Massenspektrometrische Untersuchung der Feldionisation von Wasserdampf an Spitzen aus Wolfram, Platin und Iridium." In: *Zeitschrift für Naturforschung A* (1963). DOI: https://doi.org/10.1515/zna-1964-0306 (cit. on p. 5).

[23] S. Stauss et al. "Review on plasmas in extraordinary media: plasmas in cryogenic conditions and plasmas in supercritical fluids." In: *Plasma Sources Sci. Technol. 27 023003* (2018). DOI: https://doi.org/10.1088/1361-6595/aaaa87 (cit. on p. 5).

[24] T. J. Lewis. "Breakdown Initiating Mechanisms at Electrode Interfaces in Liquids." In: *IEEE Transactions on Dielectrics and Electrical Insulation* (2003). DOI: https://doi.org/10.1109/TDEI.2003.1255771 (cit. on p. 5).

[25] A.G. Kalinichev and S.V. Churakov. "Size and topology of molecular clusters in supercritical water: a molecular dynamics simulation." In: *Chemical Physics Letters 302* (1999). DOI: https://doi.org/10.1016/S0009-2614(99)00174-8 (cit. on p. 5).

[26] K. Grosse et al. "Nanosecond plasmas in water: ignition, cavitation and plasma parameters." In: *Plasma Sources Sci. Technol.* (2019). DOI: https://doi.org/10.1088/1361-6595/ab26fc (cit. on p. 6).

[27] M. Faraday. *The Bakerian Lecture — Experimental relations of gold (and other metals) to light*. Lecture. 1857 (cit. on p. 7).

[28] Y. Xia et al. "Shape-Controlled Synthesis of Metal Nanocrystals: Simple Chemistry Meets Complex Physics?" In: *Angew. Chem. Int. Ed. 48,1* (2009). DOI: https://doi.org/10.1002/anie.200802248 (cit. on p. 7).

[29] J. Patel et al. "Synthesis of surfactant-free electrostatically stabilized gold nanoparticles by plasma-induced liquid chemistry." In: *Nanotechnology 24* (2013). DOI: https://doi.org/10.1088/0957-4484/24/24/245604 (cit. on p. 7).

[30] A. Hamdan et al. "Plasma-surface interaction in heptane." In: *J. Appl. Phys. 113, 213303* (2013). DOI: https://doi.org/10.1063/1.4809766 (cit. on p. 8).

[31] V. Amendola and M. Meneghetti. "What controls the composition and the structure of nanomaterials generated by laser ablation in liquid solution?" In: *Phys. Chem. Chem. Phys.* (2013). DOI: https://doi.org/10.1039/C2CP42895D (cit. on p. 8).

[32] K. Sasaki and N. Takada. "Liquid-phase laser ablation." In: *Pure and Applied Chemistry* (2010). DOI: https://doi.org/10.1351/PAC-CON-09-10-23 (cit. on p. 9).

[33] M. Clupek V. Babicky and P. Lukeš. "Determination of Electrical Characteristics of Nanosecond Discharge in Liquid." In: *IEEE 19th International Conference on Dielectric Liquids (ICDL)* (2017). DOI: https://doi.org/10.1109/ICDL.2017.8124686 (cit. on p. 17).

[34] W. S. Rasband & Kevin W. Eliceiri C. A. Schneider. "NIH Image to ImageJ: 25 years of image analysis." In: *Nat Methods 9, 671–675* (2012). DOI: https://doi.org/10.1038/nmeth.2089 (cit. on p. 18).

[35] Sweden COMSOL AB Stockholm. *COMSOL Multiphysics® v. 6.1.* 1857 (cit. on pp. 24, 25).

[36] *MAE 324: The Structure and Properties of Engineering Materials, Princeton University.* Online (cit. on p. 30).

[37] M. Kim et al. "Synthesis of Nanoparticles by Laser Ablation: A Review." In: *KONA Powder and Particle Journal No. 34 80-90* (2017). DOI: https://doi.org/10.14356/kona.2017009 (cit. on p. 31).

Danksagung

An dieser Stelle möchte ich mich bei allen Menschen bedanken, die mir bei der Anfertigung meiner Bachelorarbeit geholfen haben. Insbesondere möchte ich mich bedanken bei:

- Prof. Dr. Achim von Keudell für die Möglichkeit, meine Bachelorarbeit am Lehrstuhl für Experimentalphysik II zu schreiben und für die hilfreichen Antworten auf meine vielen Fragen.
- Prof. Dr. Judith Golda für die Übernahme der Zweitkorrektur.
- Pia Pottkämper für die wirklich hervorragende Betreuung während der gesamten Arbeit, dem Anfertigen der SEM Bilder und für die Hilfe bei allen Problemen sowie dem Korrekturlesen.
- Dr. Katharina Laake für die ausführliche Einführung in den Versuchsaufbau, die Möglichkeit der Laserablation bei der Firma Lidrotec GmbH.
- Elia Jüngling für die gute Zusammenarbeit im Projekt B7 und für die Erstellung der Simulation der Elektrodenspitze sowie Lara Boeddinghaus für die angenehme Arbeitsatmosphäre im Büro.
- Paolo Cignoni für das Erstellen der TEM Bilder und die Erklärungen, wie das TEM überhaupt funktioniert.
- Allen Mitgliedern des Lehrstuhls EP2 für die freundliche Aufnahme in ihre Gruppe.
- Ein riesiges Dankeschön möchte ich meiner Familie und meinen Freunden aussprechen, die mich während des gesamten Studiums unermüdlich motiviert und unterstützt haben. Insbesondere bedanke ich mich bei meinen Eltern Beate und Heinrich, meiner Schwester Anja sowie bei meinen Großteltern.

Ad maiorem Dei gloriam